Anisotropic Hydrogel Degradation Enhances 3D Collective Cell Alignment, Mechanotransduction and Osteogenic Differentiation

Claudia A. Garrido[1,2], Daniela S. Garske[1], Christian H. Bucher[1], Shahrouz Amini[2], Georg N. Duda[1], Katharina Schmidt-Bleek[1], Amaia Cipitria[2,3,4 (*)]

[1] Julius Wolff Institute for Biomechanics and Musculoskeletal Regeneration, Berlin Institute for Health at Charité – Universitätsmedizin Berlin, Berlin, Germany

[2] Max Planck Institute for Colloids and Interfaces, Potsdam, Germany

[3] Group of Bioengineering in Regeneration and Cancer, Biogipuzkoa Health Research Institute, San Sebastián, Spain

[4] IKERBASQUE, Basque Foundation for Science, Bilbao, Spain

(*) Correspondence: Amaia Cipitria, amaia.cipitriasagardia@bio-gipuzkoa.eus; amaia.cipitria@mpikg.mpg.de

Keywords: 3D patterned degradation, anisotropic dual crosslinking, alginate, primary human mesenchymal stromal cells (hMSC), collective cell alignment, osteogenic differentiation, mechanotransduction, YAP expression, YAP nuclear translocation

Abstract

Tissue engineering involves assembling cells and mimicking the complex anisotropic architecture of biological tissues to perform specific functions. This study explores the impact of patterned hydrogels with anisotropic degradation compared to single-phase materials on the potential of enhancing cell spreading, collective alignment, mechanotransduction and osteogenic differentiation of encapsulated human mesenchymal stromal cells (hMSCs). Spatial patterns of degradable (Deg)

and non-degradable (noDeg) subregions are formed by photolithography: UV-triggered thiol-ene crosslinking with matrix metalloprotease (MMP) sensitive peptides form Deg phases, while non-UV exposed regions result in Diels-Alder spontaneous click crosslinking and noDeg phases. 3D patterns in hydrogel degradation enhance hMSC spreading and allow collective cell alignment in Deg areas, while cells remain rounded with no alignment in noDeg regions. In addition, we observe a boosted osteogenic differentiation when compared to single-phase materials, as mid osteogenic markers (osteocalcin) are expressed at day 14 in anisotropic gels, whereas in single-phase only early osteogenic markers are found (osterix). Mechanosensing pathways were evaluated using the expression and localization of YAP. Deg sections in patterned materials have an enhanced nuclear translocation and higher YAP expression compared to single-phase Deg materials and noDeg sections. This effect is lost and no patterns in YAP expression and localization emerge when using an MMP-scramble peptide or no-RGD materials. These findings demonstrate that 3D patterns in alginate hydrogel degradation guide hMSC spreading, collective alignment, enhance YAP nuclear translocation and osteogenic differentiation. Mimicking tissue anisotropy in 3D patterned hydrogels could have broad applications in biofabrication and tissue engineering.

Statement of significance

Patterned materials integrate multiple characteristics within a single material, closely mimicking the anisotropy found in tissues. This research goes further by demonstrating how anisotropic degradation of cell-laden hydrogels leads to emerging patterns in mechanics. As a consequence, anisotropic hMSC morphology and collective alignment are shown in 3D patterned materials compared to single-phase counterparts. Additionally, we show enhanced and spatially guided hMSC osteogenic differentiation in patterned materials. Furthermore, anisotropic mechanosensing via YAP/TAZ signaling is shown to mediate this enhanced and spatially guided mechanotransduction and osteogenic differentiation. Finally, we explore how additional biochemical stimuli can further boost the spatially guided hMSC osteogenic differentiation. These findings advance our understanding of cell response in anisotropic microenvironments, with broad applications in biofabrication and tissue engineering.

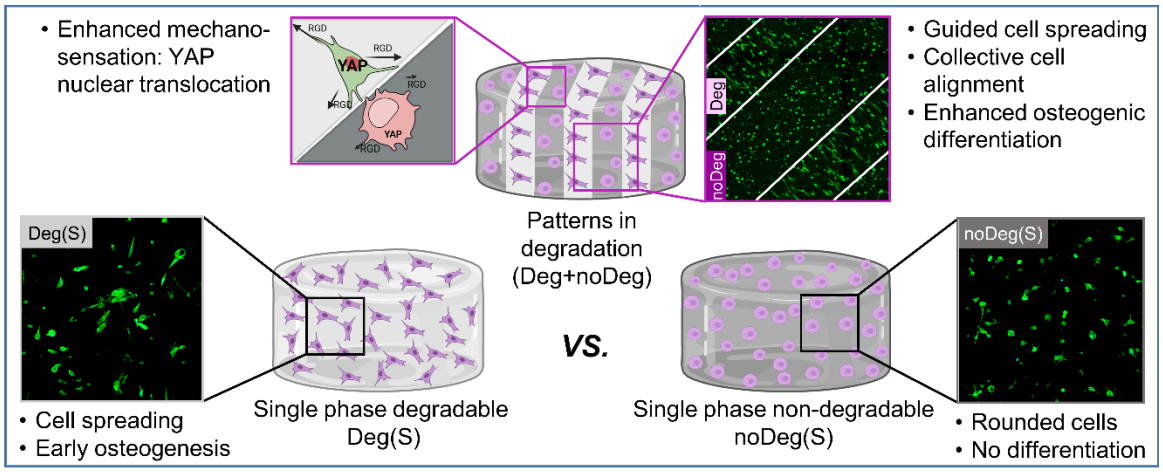

Figure 0: Graphical abstract

54 **1 Introduction**

55 Tissue engineering involves assembling cells and mimicking the complex anisotropic architecture of
56 biological tissues to perform specific functions. The use of human mesenchymal stromal cells
57 (hMSCs) is a promising approach in regenerative medicine [1], due to their self-renewal, clonality
58 (proliferation from a single cell) and potency (differentiation into different cell types) [2].
59 Encapsulation of hMSCs in biomaterials offers a variety of options to guide and control their
60 behavior, by modulating the local chemistry and physics provided to cells [3][4]. Hydrogels are
61 widely used biomaterials thanks to their high cytocompatibility [5] and modifiable chemistry,
62 providing tunable biophysical [6] and biochemical [7] properties. These have been shown to trigger
63 specific cell activities, such as matrix stiffness [8][9][10], viscoelasticity [11] [12], degradability
64 [13], ECM interaction by adhesion ligands [14], or ECM fiber arrangements [15]. In many cases
65 these efforts have focused on homogeneous materials in which the cells reside. However,
66 biomaterials in nature are typically anisotropic and provide a distinct architecture to cells.

67 Thus, single-phase materials can only partially provide a mimicry of the complex ECM interaction in
68 living tissues. Native ECM is anisotropic with distinct spatially segregated properties [16]. Multiple
69 phases in one matrix arranged in spatially discrete sections - patterned biomaterials - allow to mimic
70 this natural ECM anisotropy, while keeping the benefits of a well-controlled synthetic material niche.
71 The versatility of 3D patterned materials allows to tune biophysical properties and guide cell
72 behavior. For example, patterns in biomolecule presentation have been used to spatially guide cell
73 migration and alignment [17][18]. Despite their potential, the study of 3D patterned synthetic niches
74 as analogs of anisotropic tissue architecture is still limited, especially how patterns in degradation can
75 influence cell behavior. Degradable patterned microchannels have been used to guide endothelial cell
76 sprouting [19], endothelium formation [20] and cell invasion [21] [22]. For other cell types, such as
77 fibroblasts [23] or hMSCs [24], materials with patterns in degradation and stiffness have been studied

78 in 3D. However, the effect of patterned matrix degradation, without the influence of other
79 biophysical/biochemical factors, in controlling encapsulated cell behavior in multicompartment
80 materials has not been fully elucidated yet.

81 The mechanisms underlying cell-matrix interactions in 3D degradable materials are traction forces
82 [25] that interact with the dynamic matrix and newly opened space due to degradation [24]. It has
83 been previously shown that degradable materials favor a spread cell morphology [26] and MSC
84 osteogenic differentiation [27]. The traction forces and integrin-mediated cell interactions in
85 degradable materials are regulated through mechanosensing pathways. Yes-associated protein (YAP)
86 and transcriptional coactivator with PDZ-binding motif (TAZ) represents one of such pathways and
87 enables nuclear mediators of mechanical signals exerted by the ECM and cytoskeletal tension [28].
88 The activation of this pathway is linked to the integrins on the cell surface and the associated traction
89 forces with the anchoring points in the ECM (e.g. binding motifs) [29]. This, in turn, is modulated by
90 the dimensionality and the degradability of the ECM [30]. YAP/TAZ expression and nuclear
91 translocation as a consequence of cytoskeletal tension, and its effect on cell differentiation [31], cell
92 communication [32] or cell polarization through spatial heterogeneity in YAP activation [33] are well
93 known. However, the influence of multicompartment materials in YAP-mediated
94 mechanotransduction requires further research.

95 Here, we investigate how 3D patterns in alginate hydrogel degradation affect hMSC behavior and
96 how multicompartment materials differ from single-phase materials. In particular, we induce hMSC
97 spreading, collective alignment, enhanced YAP nuclear translocation and osteogenic differentiation
98 solely with anisotropic hydrogel degradation and under standard cell growth media. Such effect is
99 enhanced under osteogenic media. Additionally, we explore the mechanisms driving osteogenesis in
100 3D patterned materials, particularly YAP nuclear translocation, and show that both matrix adhesion
101 and degradation characteristics are a necessary requirement. These results advance our understanding

102 of cell response in anisotropic microenvironments. Mimicking tissue anisotropy in 3D patterned
103 hydrogels could have broad applications in biofabrication and tissue engineering.

104 2 Materials and Methods

105 2.1 Alginate modification

106 Norbornene and tetrazine were added to the alginate backbone via carbodiimide chemistry (see Fig.
107 1A). The alginate used was low molecular weight, high guluronic acid sodium alginate (MW 75 kDa
108 Pronova UP VLVG; NovaMatrix). The coupling of norbornene (N, TCI Chemicals, #N0907) and
109 tetrazine (T, Conju-probe, #CP-6021) to the alginate molecule was performed as previously
110 described [23]. Alginate modification with norbornene was performed with a theoretical degree of
111 substitution (DS_{theo}) of 500. Alginate modification with tetrazine was performed with a DS_{theo} of 170
112 (Suppl. Table S1). NMR spectroscopy was used to determine the actual DS (DS_{actual}) (Suppl. Fig.
113 S1). The quantification of the DS was performed by averaging the characteristic peak area: for
114 tetrazine 10.2, 8.2 and 7.4 ppm and for norbornene 6.2-5.8 ppm, then dividing this value by the area
115 of the characteristic alginate peak (G-1) between 5.2-4.8 ppm. NMR measurements were performed,
116 using a 1.5 % w/v alginate solution in deuterium oxide (64 scans; Agilent 400 MHz Premium
117 COMPACT equipped with Agilent OneNMR Probe) and analyzed using MestreNova Software
118 (version 12.03).

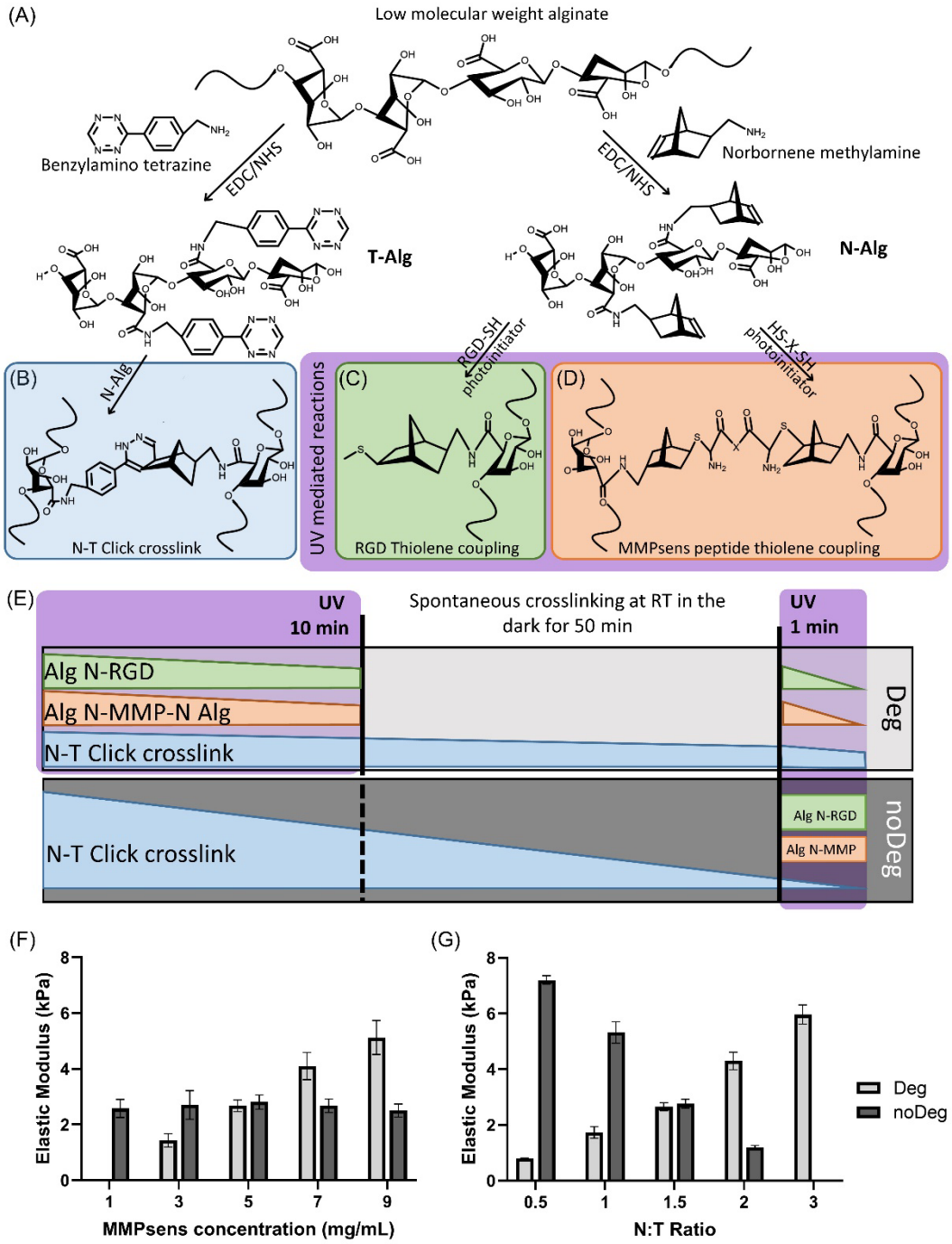

Figure 1: Description of the material chemistry. *Scheme of the carbodiimide coupling of norbornene or tetrazine groups to the alginate backbone (A). Scheme of non-degradable bonds through Diels-Alder spontaneous click crosslinking of norbornene and tetrazine (B, blue). UV light dependent thiol-ene reactions of norbornene groups with RGD (C, green) and MMPsens peptide*

124 *crosslinker (X: GCRD-VPMS ↓ MRGG-DRCG) (D, orange). Time scheme depicting the different*
125 *reactions occurring during the dual crosslinking (E). Material elastic modulus can be tuned through*
126 *the MMPsens concentration, for a constant N:T ratio of 1.5 (F) and also through varying the N:T*
127 *ratio, for a constant MMPsens concentration of 5mg/mL (G).*
128

129 **2.2 Isolation and culture of primary human bone-marrow derived mesenchymal stromal cells**
130 **(hMSCs)**

131 Bone-marrow derived hMSCs (female, 50 years, no secondary diagnosis, no co-medication) were
132 received from the Core-Facility "Cell Harvesting" of the Berlin Institute of Health (BIH). The cells
133 were isolated from metaphyseal bone marrow biopsies from patients undergoing hip replacement at
134 the Charité - Universitätsmedizin Berlin, as previously described [34][35]. Written informed consent
135 was given, and ethics approval was obtained from the local ethics committee/institutional review
136 board (approval number EA2/089/20) of the Charité – Universitätsmedizin Berlin.

137 For differentiation analyses, hMSCs in passage P5 were encapsulated in hydrogels and incubated in
138 growth or osteogenic media. For further information on cell isolation and cell culture procedures,
139 please refer to Supplementary Information 1.

140 **2.3 Fabrication of anisotropic matrices: 3D patterns in alginate hydrogel degradation**

141 Hydrogels were fabricated based on previously established protocols [23]. The single-phase materials
142 (no photo mask) were used as controls for mechanical testing of bulk properties by rheology with a
143 frequency sweep test (Section 2.4.1), and for cell stainings. In addition, 3D patterned hydrogels were
144 generated as described below. For all material samples, cell culture was performed either in growth
145 or osteogenic.

146 **2.3.1 Non-degradable matrix: Diels-Alder click-crosslinking**

147 The precursors for the hydrogel were dissolved in phosphate-buffered saline (Merck #D8537) and
148 distributed into 2 tubes. The first tube contained norbornene-modified alginate (N-alg); MMP-
149 sensitive (MMPsens) peptide (GCRD-VPMS ↓ MRGG-DRCG, 95 % purity; WatsonBio) at a final
150 concentration of 5 mg/ml of hydrogel, thiolated RGD-peptide (CGGGGRGDSP; Peptide2.0) at a
151 theoretical concentration of 5 molecules of RGD per alginate chain (DS 5, 1.2×10^{-3} mM), and the cell
152 suspension at final concentration of 2×10^{6} cells/mL of hydrogel. The second tube contained tetrazine-
153 modified alginate (T-alg) and the photoinitiator (Irgacure 2959; Sigma-Aldrich, #410896) at a final
154 concentration of 3 mg/mL of hydrogel. The total final concentration of alginate was 2 % w/v at a N:T
155 ratio of 1.5. Despite MMPsens and the photoinitiator being present, these were not activated due to
156 the lack of UV exposure. Nevertheless, the MMPsens and photoinitiator need to be present to allow
157 for patterned materials (see Section 2.3.3).

158 The two solutions were mixed by pipetting and cast onto a bottom glass plate (borosilicate glass,
159 Filafarm, #1000185), with the casting area being restricted on three sides by glass spacers
160 (Marienfield, #1100420), and immediately covered with a glass slide previously treated with
161 SigmaCoat (≥ 99.5 %; Sigma-Aldrich, #SL2) to prevent adhesion. The gel height was constrained to
162 2 mm by the thickness of the glass spacers. Spontaneous click-crosslinking for 60 min at room
163 temperature (RT) and in the dark allowed Diels-Alder crosslinking and the N:T covalent bonds to
164 form (Fig. 1B).

165 In order to ensure a homogeneous binding of the RGD-peptide, crosslinked gels were subsequently
166 exposed to 2 min UV light (365 nm) at 10 mW/cm^2 (Omnicure S2000) in a custom-built exposure
167 chamber. The RGD-peptide binds to the free norbornenes via thiol-ene reaction (Fig. 1C). The
168 cylindrical hydrogels were punched from the cast gel sheet using 5 mm biopsy punches (Integra

169 Miltex) and incubated in cell culture media at 37 °C and 5 % CO_2. Further information on the
170 reaction timeline can be found in Fig. 1E.

171 **2.3.2 Degradable matrix: UV-mediated thiol-ene crosslinking with MMPsens peptide**

172 The production of degradable materials followed the same procedure as described in Section 2.3.1,
173 with an additional step for the MMPsens peptide crosslinking. After casting the hydrogel solution
174 between the glass plates, the material was immediately exposed to UV light at 10 mW/cm^2 for 10
175 min to initiate the coupling of the degradable MMPsens peptide to the norbornene-modified alginate
176 via thiol-ene crosslinking (Fig. 1D). After the UV exposure, the materials were placed for an
177 additional 50 min at RT in the dark to allow for the N:T covalent bonds to be formed. To ensure a
178 homogenous binding of RGD, the hydrogels were finally exposed again to UV for 2 min (Fig. 1C).
179 Further information on the reaction timeline can be found in Fig. 1E. Hydrogels were punched out
180 and incubated in cell culture media at 37 °C and 5 % CO_2.

181 The mechanical properties (measurement method described in Section 2.4) can be modulated by
182 varying the concentration of MMPsens peptide (Fig. 1F) and by tuning the N:T ratio (Fig. 1G). For a
183 constant N:T ratio of 1.5, the non-UV exposed noDeg regions have a constant elastic modulus, while
184 the UV exposed Deg regions results in stiffer matrices with increasing MMPsens peptide
185 concentration (Fig. 1F). In contrast, for constant MMPsens peptide concentration of 5 mg/mL, the
186 non-UV exposed noDeg regions have a decreasing elastic modulus with increasing N:T ratio, while
187 the UV exposed Deg regions results in stiffer matrices with increasing N:T ratio, due to the greater
188 abundance of N-alg available for the thiol-ene crosslinking (Fig. 1G)

189 **2.3.3 Anisotropic matrix: Photolithography of patterned dual crosslinked hydrogels**

190 The creation of patterned materials followed the same procedure as described in Section 2.3.2, with
191 the addition of a photomask placed on top of the cover glass during the UV mediated thiol-ene

192 coupling of the MMPsens peptide. The photomask had a pattern of straight lines with 500 µm
193 thickness (UV light blocking sections, non-degradable matrix equivalent to 2.3.1) placed 300 µm,
194 500 µm or 800 µm apart (UV light permitting sections, degradable matrix equivalent to 2.3.2). After
195 the 10 min UV exposure through the photomask, followed by 50 min incubation in the dark at RT, in
196 which all the N-T bonds were formed and no additional grafting of MMP occurred, crosslinked gels
197 were exposed to 2 min UV light at 10 mW/cm^2 without a photomask for homogeneous binding of the
198 RGD-peptide (Fig. 1E).

199 Two additional control materials are included in this manuscript: materials with a non-degradable
200 peptide sequence and materials with no RGD adhesion peptide. The control materials with a non-
201 degradable peptide sequence were achieved by replacing the MMPsens with the homologous
202 scramble (MMPscr) peptide (GCRD-VpMS ↓ mRGG-DRCG, 95 % purity; WatsonBio), where the
203 amino acids in lower case were switched for the D-isoform, unrecognizable by MMP enzymes. For
204 the control materials with no adhesion peptides, the thiolated RGD solution was replaced with PBS.
205 All of the controls follow the procedure established under section 2.3.3.

206 **2.4 Hydrogel mechanical characterization over time**

207 Mechanical characterization was performed on day 1 and day 14. All mechanical characterization
208 was performed with cell-laden materials to quantify the effect of cell-driven enzymatic degradation
209 of the hydrogels. The material degradation and changes in mechanical properties were evaluated via
210 two different methods: (i) rheology with a frequency sweep test to measure the bulk shear modulus,
211 G (and then calculate the elastic modulus, E), (ii) microindentation to measure the surface elastic
212 modulus of single-phase and patterned materials, and display the iso- or anisotropic values with a
213 surface map.

2.4.1 Rheology

Storage and loss modulus of single-phase hydrogels were determined with a rheometer (Anton Paar MCR301) via frequency sweeps with a parallel plate geometry of 8 mm (PP08, Anton Paar). The frequency sweep was performed from 0.01 to 10 Hz and at 0.1 % shear strain at RT (n = 6). Once contact with the gel surface was established, a pre-compression of 10 % of the height of the hydrogel was applied prior to the measurement. No additional hydration was needed as the experiment lasted less than 10 min. To obtain the elastic modulus, first the shear modulus (G) was derived from the storage (G') and loss (G") modulus using Rubber's elasticity theory $G = \sqrt{G'^2 + G''^2}$ [36]. The elastic modulus (E) was calculated using the values of G and the approximation of Poisson's ratio (ϑ) equal to 0.5, $E = 2G\ (1 + \vartheta)$ [37]. The mesh size (ξ) was approximated based on storage modulus G' in low frequencies (0.1-1Hz), $\xi = \sqrt[3]{6RT/G'\pi\ N_{av}}$, as previously described [38].

2.4.2 Microindentation

To verify the emerging patterns in mechanical properties of the 3D hydrogels due to anisotropic degradation, the surface elastic modulus of the materials on day 1 and day 14 was mapped into a heatmap. Depth-sensing microindentation measurements were done using a Triboindenter TI-950 (Hysitron-Bruker, MN, USA) with a cono-spherical tip of 50 µm radius. The tip was calibrated by an air indent, followed by a quick approach to detect the surface. Similar procedures as previously described were used [23], but were adapted for softer materials. Then, the measurements were automatized as follows: ~350 µm retraction, an indent approach of ~150 µm and strain rate of ~30 µm/s. The measurements were done in automated mode to map a 2 x 2 mm^2 area with 10 x 10 indents and 200 µm spacing. To ensure that the sample remained hydrated during the measurement, the samples were fixed to a sponge and partially submerged in PBS.

236 To obtain the elastic modulus from the load-displacement indentation curves, the Hertzian contact
237 model was used. The analysis of the load-displacement curves was automated by a custom-made
238 Python3 script. We used an adapted version of the script described in our previous work [23], related
239 to the selection of the origin point. The origin point is the initial contact point where the tip gets in
240 contact with the material surface and from which the Hertzian model will be determined. This
241 procedure was previously automatized by mathematically determining the minimum of the first part
242 of the indentation curve. However, in very soft materials like the ones presented in this study, the
243 origin point could not be identified using the previous method, as the initial contact point was not as
244 clear as with stiffer gels. The adapted version of the script allows the user to select the origin point
245 manually.

246 **2.5 Characterizing volume and wet weight changes over time**

247 To track the degradation of single-phase materials, volume changes, wet weight changes and swelling
248 ratios (S_t) were tracked over time, at 0 (after 2 h equilibration), 1, 3, 5, 7, 14, 21 and 28 days. At each
249 time point, single-phase hydrogels were weighed under sterile conditions and measured using a
250 caliper. The volume was determined assuming a cylindrical shape, calculated from one height
251 measurement and the mean of two diameter measurements. Swelling (S) was calculated with the
252 equation $S_t=W_t/W_{t=0}$, where W_t refers to the hydrogel wet weight at a given time point t, and $W_{t=0}$
253 refers to the hydrogel wet weight at the initial time point.

254 **2.6 Primary hMSC viability and cell number**

255 To verify cell viability Live/Dead stainings were performed after 1 and 14 days. The hydrogels were
256 taken out from the incubation media and washed with PBS (Merck #D8537). Then the cells were
257 stained with a solution of 4 µM Calcein AM (Biomol Bioquest #ABD-22002, 500x solution in
258 DMSO) and 4 µM Ethidium homodimer-1 (Sigma #E1903, dilution 1:1000 from original solution)

259 dissolved in PBS to identify live and dead cells, respectively. The staining solution volume was 400
260 µl per hydrogel in a 24 well plate, stained for 12 min in a cell culture incubator at 37 °C, 5 % CO_2 in
261 the dark. A final washing step was performed with 400 µl of PBS per hydrogel at RT for 5 min and
262 protected from light.

263 Imaging was performed on a confocal microscope (Leica SP5, Germany). Quantification of cell
264 number and viability at each time point was performed using ImageJ software (ImageJ 1.53s) [39].
265 One position from 3 independent samples was acquired at the gel center at 10x water-immersed
266 objective (HCX APO L U-V-I 10.0x 0.30), with tile merging of 3x3 and a 250 µm z-stack.

267 **2.7 Primary hMSC morphology**

268 Cell morphology was assessed after 1 and 14 days, staining the nuclei and actin cytoskeleton using
269 SYTOX and Phalloidin, respectively. All steps were performed under orbital shaking in a 24 well
270 plate and using a volume of 500 µL per gel. The culture media was removed and the gels were
271 washed twice with PBS (Merck #D8537). Then, the encapsulated cells were fixed in 4 %
272 paraformaldehyde solution (Sigma-Aldrich, #158127) for 45 min at RT, followed by
273 permeabilization with 0.3 % Triton X-100 (Sigma-Aldrich, #11488696) for 15 min, washed twice
274 with 3 % bovine serum albumin (BSA, Sigma-Aldrich, #A7906) in PBS for 5 min. The staining
275 solution was dissolved in PBS containing 0.1 % TritonX-100 and 3 % BSA and with the following
276 concentrations: 0.5 µM SYTOX (Thermo Fisher, #S11381) and 1 µg/mL of Phalloidin 405
277 Conjugate (CruzFluor™, #SC363790). The staining was performed protected from light, during 4 h
278 at RT. Final washing was performed twice with 3 % BSA in PBS for 5 min at RT.

279 For imaging, three different positions per gel were acquired at the gel center from two independent
280 samples using a confocal microscope (Leica SP5, Germany). For a general quantification of cell

281 morphology, 10x water-immersed objective (HCX APO L U-V-I 10.0x0.30), with a tile merging of
282 2x2 was used and a 250 µm z-stack.

283 **2.8 Primary hMSC differentiation**

284 Cell differentiation was tested using Osterix (OSX) as an early osteogenic differentiation (see section
285 2.9), Osteocalcin (OCN) as medium osteogenic differentiation (see section 2.9), and OsteoImage as
286 late osteogenic differentiation marker. The stainings were performed after 14 days, always in
287 combination with cell morphology staining, SYTOX and Phalloidin, as described in Section 2.7.

288 For OsteoImage (Lonza, #PA1503) the staining procedure followed the provider´s instructions.
289 Briefly, the fixed cells (see section 2.7) were washed with the wash buffer twice for 5 min. Then, the
290 previously diluted 1:100 Osteoimage staining reagent in dilution buffer was added to the gels, 500 µL
291 per gel. The incubation was carried out at 4 °C, overnight and protected from light. The next day, the
292 samples were washed three times with the wash buffer and then imaged.

293 For imaging, three different positions per gel were acquired at the gel center from two independent
294 samples using a confocal microscope (Leica SP5, Germany). For a higher magnification
295 quantification of cell morphology, 25x water-immersed objective (HCX IRAPO L 25.0x0.95), with a
296 tile merging of 4x4 was used and a 250 µm z-stack.

297 **2.9 Immunostainings**

298 YAP, Osterix (OSX) and Osteocalcin (OCN) expression was evaluated by immunofluorescence.
299 After performing the morphological staining, SYTOX and Phalloidin, as described in Section 2.7, the
300 primary antibody was incubated for 24 h at 4 ºC under constant rocking. The antibodies used were:
301 YAP IgG2aκ mouse monoclonal (Santa Cruz, #sc-101199) at 10 µg/mL in PBS, OSX polyclonal
302 rabbit (abcam, ab22552) 10 µg/mL in PBS-1%BSA and OCN monoclonal mouse IgG1 (R&D

303 Systems, #MAB1419) at 25 µg/mL in PBS. After the primary antibody staining, the samples were
304 washed three times with 400 µL of 3 % BSA in PBS for 30 min. The secondary antibody
305 (ThermoFisher, #A32728) was stained for 2 h at RT under constant rocking. Finally, the samples
306 were washed 3 times with 3 % BSA in PBS and imaged.

307 For imaging, three independent positions per gel were acquired at the gel center from two
308 independent samples using a confocal microscope (Leica SP5, Germany). For a higher magnification
309 quantification of cell morphology, 25x water-immersed objective (HCX IRAPO L 25.0x0.95), with a
310 tile merging of 4x4 was used and a z-stack of 250 µm.

311 **2.10 Quantitative analysis of stained sections**

312 The cell morphology in 3D patterned materials was evaluated using a previously described macro
313 [23] written in ImageJ (ImageJ 1.53s, [39]). The cell projected area, cell circularity and cell number
314 were obtained from z-stack projections. The macro offers the possibility to freely divide an image
315 into a grid, which leads to a heat map in which the results are later depicted. The cell border threshold
316 was manually set.

317 To evaluate collective cell alignment, the Image J plugin Directionality was used [40]. The graphs
318 show the 'Direction (°)' or angle vs. the 'Amount', which shows the fraction of cells with a preferred
319 direction, normalized to the total cell number.

320 YAP, Osterix (OSX) and Osteocalcin (OCN) expression was quantified as a percentage of the marker
321 expressing cells (YAP, OSX or OCN or positive cells) divided by the total cell number (SYTOX).
322 The images were evaluated using ImageJ: first, a background subtraction of a control image of the
323 staining with only the secondary antibody was performed, followed by setting manually the threshold
324 and finally evaluating with the automatic particle counting function. The mineralized area obtained

325 with OsteoImage (OI) staining, was established as a percentage by dividing the OI positive cell area
326 by the total cell area (phalloidin staining).

327 The nuclear to cytoplasmic ratio of YAP was evaluated using a previously described method [41].
328 Briefly, individual cells were segmented for nucleus (SYTOX) and cytoplasm (phalloidin) to define
329 the respective subcellular regions. Next, YAP average intensity within each subcellular region was
330 quantified and the ratio calculated.

331 **2.11 Flow cytometry analysis**

332 After 14 days of encapsulation, the cells were retrieved from the hydrogels using alginate lyase
333 (Sigma, #A1603, reconstituted in Ca/Mg-free PBS in 2mg/mL). The cells were incubated for 30 min
334 at 37C, then centrifuged at 400 rcf during 5 min and washed twice with PBS. The flow cytometry
335 staining and analysis was done as described before [42]. The viable cells were determined using
336 fixable live/dead blue staining kit for UV excitation (Thermo Fisher L34962). The blocking solution
337 (FcX, BioLegend, 422301) was used to prevent unspecific binding. Staining with antibodies
338 (Supplementary table 2) was performed on ice and using flow cytometry buffer (phosphate-buffered
339 saline (PBS) including bovine serum albumin (0.5% w/v) and sodium acid (0.1% w/v)). Fixation and
340 permeabilization kit (BioLegend, 426803) was used for intracellular staining, while intranuclear
341 staining was performed with the TrueNuclear Transcription Factor buffer set (BioLegend, 424401)
342 according to the manufacturer's protocol. The stained cells were analyzed on an LSR Fortessa
343 (SORP, Biosciences, USA) system by applying a bead-based compensation matrix ID7000 spectral
344 flow cytometry (Sony Biotechnology, San Jose, CA, USA) with individual autofluorescence
345 unmixing. Gating and analysis of the population were performed with FlowJo software (BD
346 Biosciences, Franklin Lakes, NJ, USA), further analysis were performed in R Statistical Software
347 (v4.4.1; R Core Team 2024) using the Spectre packages [43].

348 **2.12 Statistical analysis**

349 Statistical analysis was performed with GraphPad Prism 8 (version 8.4.3 for Windows, GraphPad
350 Software Inc., Boston, Massachusetts USA). To test for normality, the Shapiro-Wilk test was applied.
351 For normally distributed data, bar plots showing mean and standard deviation (SD) were used and the
352 statistical comparison was performed using ANOVA (* alpha < 0.05, ** alpha<0.01 or ***
353 alpha<0.001), corrected with Bonferroni test for multiple comparisons. For not normally distributed
354 data, box plots with median, 1st and 3rd quartile were used and data was compared using a Kruskal-
355 Wallis test (* alpha < 0.05, ** alpha<0.01 or *** alpha<0.001), corrected with Dunn´s test for
356 multiple comparisons

357 **3 Results**

358 **3.1 Anisotropic degradation of cell-laden patterned hydrogels leads to emerging patterns in**
359 **mechanics**

360 Cells were encapsulated in photopatterned alginate hydrogels (Fig. 2A) with initial homogeneous
361 mechanical properties (Fig. 2J). The comparable mechanical characteristics of the materials were
362 achieved by tuning the MMPsens peptide concentration (Fig. 1F) and the N:T ratios (Fig 1G). The
363 mechanical properties of cell-laden hydrogels evolved during time due to the cellular enzymatic
364 action (Fig. 2A). Those mechanical properties were characterized by rheology (Fig. 2B, C, D, G) and
365 microindentation (Fig. 2H-J).

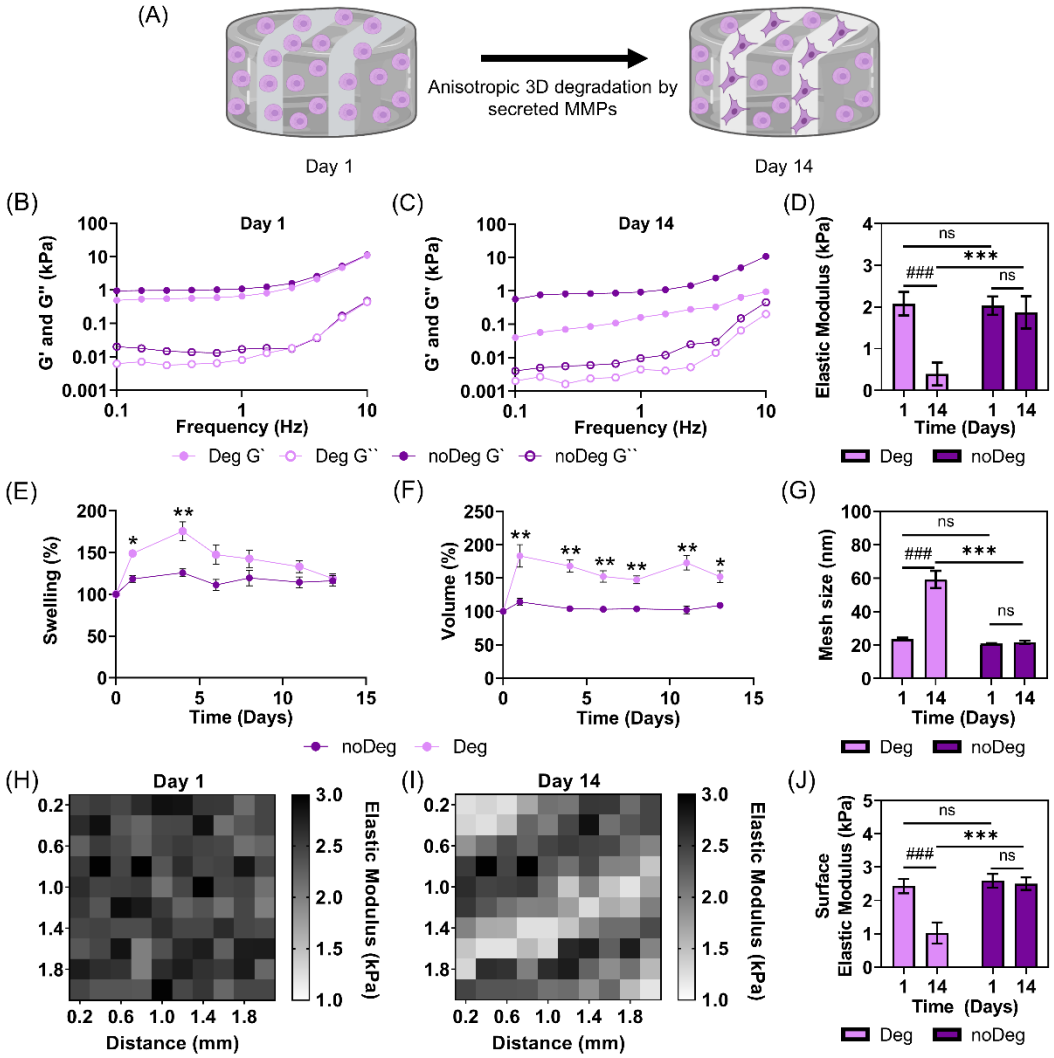

Figure 2: Changes in mechanical properties and swelling over time of cell-laden anisotropic hydrogels. *Anisotropic dual crosslinking results in 3D patterns of hydrogel degradation due to cell-derived enzymatic action (A). Representative plots of G′ (storage modulus, ●) and G′′ (loss modulus, ○) obtained by rheology of noDeg single-phase (dark purple) and Deg single-phase (light purple) materials, on day 1 (B) and day 14 (C) from n=6 gels. Elastic modulus (D) and corresponding mesh size (G), approximated from rheology data. Swelling (E) and volume (F) changes over time (relative to 2h after equilibration), from n=3 gels. Representative microindentation map of the surface elastic modulus on day 1 (H) and day 14 (I), 10x10 grid, indentation spacing of 200 µm. Surface elastic modulus in Deg and noDeg phases obtained by microindentation, averaging all indents in a specific*

region of patterned materials on day 1 and day 14 (J). Statistical significance with ANOVA and Bonferroni correction.

The degradable and non-degradable materials have comparable values of loss (G′) and storage (G′′) modulus on day 1 (Fig. 2B). However, on day 14 there is a pronounced difference in G′ and G′′ for Deg materials (Fig. 2C). A significant decrease over time in mechanical properties of Deg materials is observed, whereas the noDeg materials preserve their elastic modulus (Fig. 2D). The elastic modulus on day 1 of Deg (2.07 ± 0.28 kPa) is comparable to noDeg (2.03 ± 0.22 kPa). Significant differences can be seen between the elastic modulus of Deg (0.39 ± 0.27 kPa) and noDeg (1.87 ± 0.38 kPa) on day 14. The elastic modulus changes can be related to the water content as there is a significant difference in the swelling (Fig. 2E) and volume changes over time (Fig. 2F), which is also reflected in an increasing mesh size (Fig. 2G). The mesh size of Deg materials increases significantly between day 1 (24 ± 1 nm) and day 14 (59 ± 5 nm), whereas in noDeg materials the mesh size remains unchanged from day 1 (21 ± 0.3 nm) to day 14 (22 ± 1 nm).

Compared to the degradation behavior of single-phase materials, the corresponding phases in patterned materials show similar characteristics, as shown by the average surface elastic modulus of microindentation measurements (Fig. 2J). As seen in the representative surface map of elastic modulus, the pattern in degradation emerges over time. There is no distinct pattern of the surface elastic modulus on day 1 (Fig. 2H), with values fluctuating around 2.5 kPa, consistent with the comparable bulk elastic modulus of both single-phase materials (Fig. 2D). However, on day 14 (Fig. 2I), there are softer sections (1-1.5 kPa) corresponding to the Deg zones and stiffer sections (2.5 kPa) associated with noDeg zones.

3.2 Anisotropic hMSC morphology and collective cell alignment in 3D patterned materials compared to single-phase counterparts

399 hMSCs were encapsulated in 3D anisotropic materials with patterns in degradation. The viability and
400 cell number were evaluated using Calcein/ EtHD1 staining. Cell viability (fraction of Calcein (+)
401 cells) remained high on day 1 (Suppl. Fig. S2A-B) and day 14 (Suppl. Fig. S2D-E) and there were no
402 visible patterns in cell viability. Cell proliferation was also evaluated by individual quantification of
403 the average cell number (total cells, Calcein and EtHD1) (Suppl. Fig. S2C and S2F).

404 Next, we investigated the effect of patterned hydrogels on cell morphology and collective alignment.
405 Patterned materials with dimensions of 500 µm:500 µm for Deg:noDeg (Fig. 3A) were compared on
406 day 14 to single-phase materials (Fig. 3E, 3G). On day 1 (Suppl. Fig. S3A-C), cell morphology was
407 similar among the two phases of the patterned material, not showing any significant differences,
408 neither in projected cell area (Fig. 3H) nor in circularity (Fig 3I). Patterns in cell morphology were
409 visible on day 14 (Fig. 3A) and were quantified through heatmaps (Fig 3B-C). The results showed
410 increased projected cell area (Fig. 3B) and decreased circularity (Fig. 3C) in Deg regions, while cells
411 remained round and with smaller projected cell area in noDeg zones. Similar trends were observed in
412 equivalent single-phase materials (Fig. 3D-G). However, the effect in the morphological changes was
413 significantly enhanced in the Deg sections of patterned materials in contrast to the single-phase Deg
414 (Fig. 3H-I).

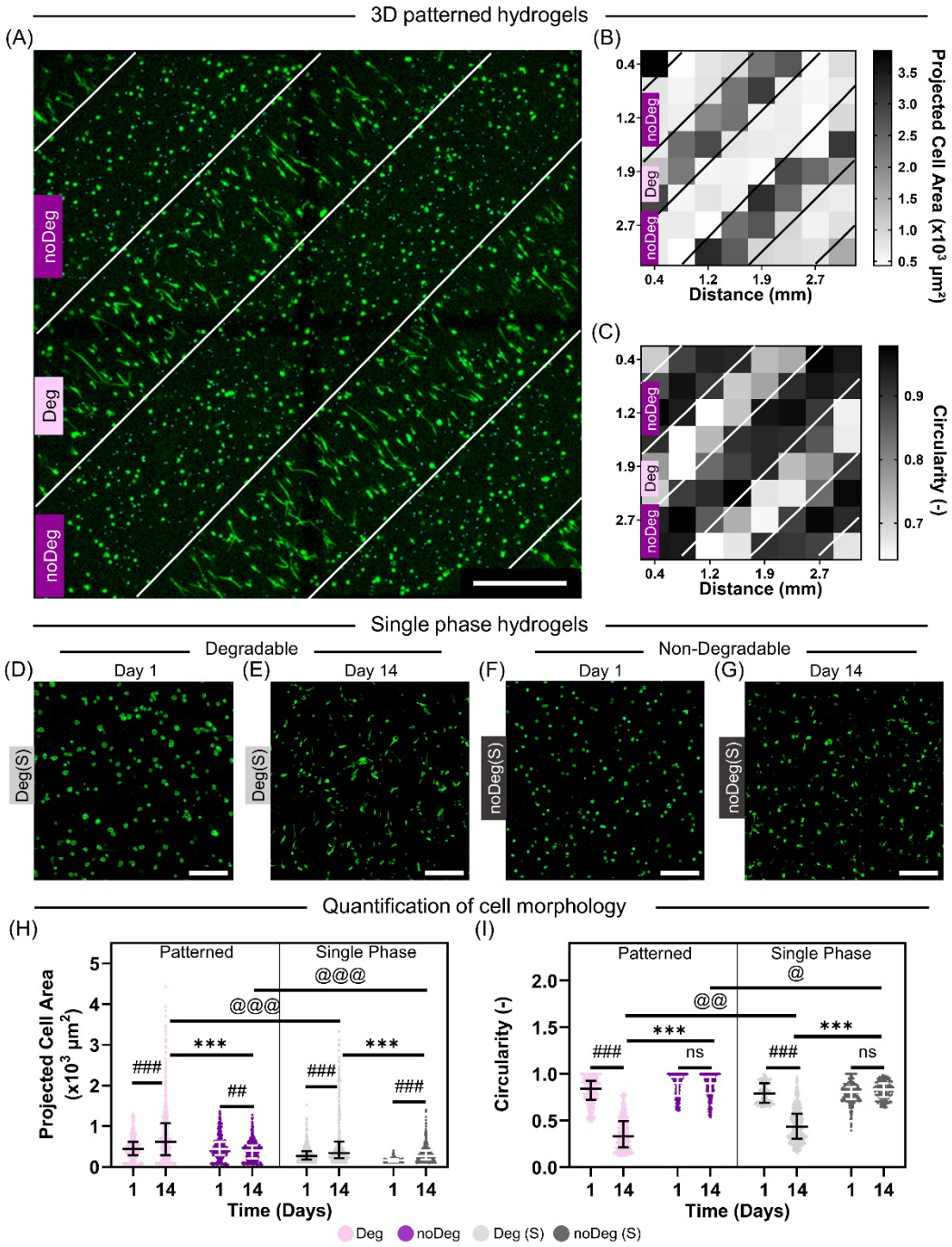

Figure 3: Anisotropic hMSC morphology in patterned materials on day 14. *Representative confocal images of actin (Phalloidin/green) and nucleus (SYTOX/cyan) staining of patterned materials with hMSCs in growth media (A). Heatmap quantification with an 8x8 grid of projected cell area (B) and cell circularity (C). Single-phase materials representative confocal images of actin*

420 *(Phalloidin/green) and nucleus (SYTOX/cyan) staining on day 1 (Deg (D) and noDeg (F)) and day*
421 *14 (Deg (E) and noDeg (G)). Dot graph of raw data (> 400 single cells per phase and condition) of*
422 *projected cell area (H) and circularity (I) on day 14 (see Suppl. Fig. S3A-C for corresponding*
423 *images and heat maps on day 1). Statistical significance with Kruskal-Wallis and Dunn's*
424 *correction). Scale bar: 500 µm (A) and 250 µm (D-G).*

425 The patterned materials allowed enhanced changes in cell morphology but also differences in
426 collective cell alignment (Fig. 4). The cell orientation was evaluated for patterns of different
427 Deg:noDeg dimensions, 300 µm:300 µm (Fig. 4A-C), 500 µm:500 µm (Fig. 4D-F) and 800 µm:200
428 µm (Fig. 4G-I). The 300 µm:300 µm photomask (Fig 4A) resulted in cells collectively aligned
429 perpendicular to the stripes in the Deg phases (Fig 4B), in contrast to the cells in noDeg sections (Fig
430 4C), where cells remained round and had no predominant orientation. This effect was further
431 enhanced with the 500 µm:500 µm photomask (Fig. 4D-F). However, for the 800 µm:200 µm
432 photomask (Fig 4G), with a broader degradable section, the collective cell alignment was lost (Fig.
433 4H) and was equivalent to single-phase materials (Suppl. Fig. 4A-D), where we found a spread cell
434 morphology but lacked a collective cell alignment. Similarly, no collective alignment was found in
435 patterned materials when subjected to constrained swelling in the XY direction (Suppl.Fig.4E-L).

436

437

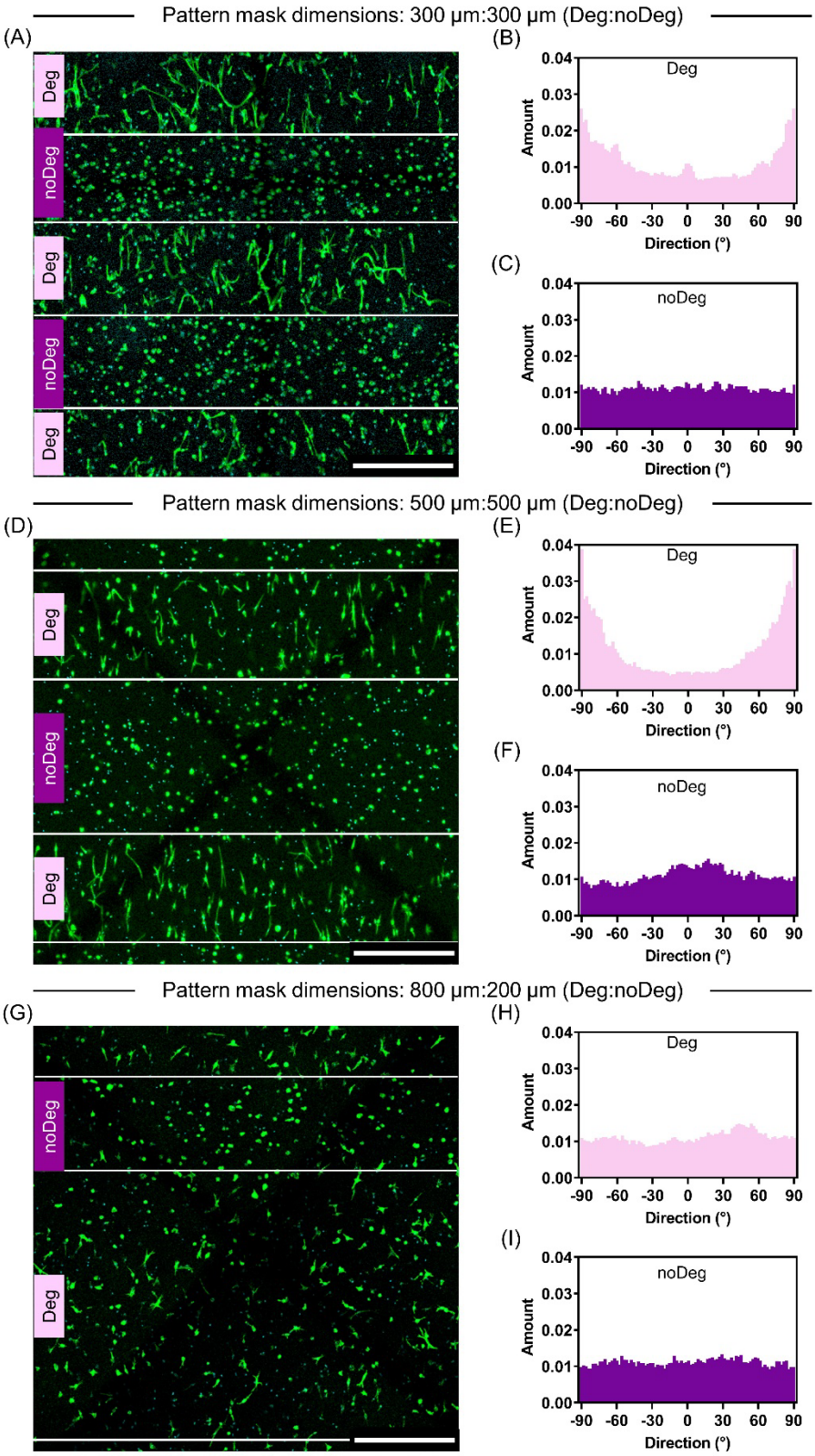
Pattern mask dimensions: 300 µm:300 µm (Deg:noDeg)
(A)
Deg
noDeg
Deg
noDeg
Deg
(B)
Deg
Amount
Direction (°)
(C)
noDeg
Pattern mask dimensions: 500 µm:500 µm (Deg:noDeg)
(D)
Deg
noDeg
Deg
(E)
(F)
Pattern mask dimensions: 800 µm:200 µm (Deg:noDeg)
(G)
noDeg
Deg
(H)
(I)

438

439 ***Figure 4: Collective cell alignment of encapsulated hMSCs in patterned materials with different***
440 ***photomask dimensions on day 14.*** *Patterned materials fabricated with photomasks of different*
441 *Deg:noDeg dimensions: 300 μm:300 μm (A-C), 500 μm:500 μm (D-F) and 800 μm:200 μm (G-I).*
442 *Representative confocal images of actin (Phalloidin/green) and nucleus (SYTOX, cyan) staining of*
443 *patterned materials with hMSCs (A, D, G) and histograms indicating the distribution of the collective*
444 *cell alignment angle in Deg and noDeg phases of patterned materials (B/C, E/F, H/I), with n > 200*
445 *cells per phase. Scale bar: 500 μm.*

446

447 **3.3 Enhanced and spatially guided hMSC osteogenic differentiation in 3D patterned**
448 **materials compared to single-phase counterparts**

449 Previous findings showed that 3D patterns in alginate hydrogel degradation induced an anisotropic
450 response in hMSC morphology and emergent properties such as collective cell alignment. This
451 motivated further investigation of the anisotropic hMSC osteogenic differentiation, evaluated by
452 early (Osterix, OSX) and intermediate (Osteocalcin, OCN) osteogenic markers.

453

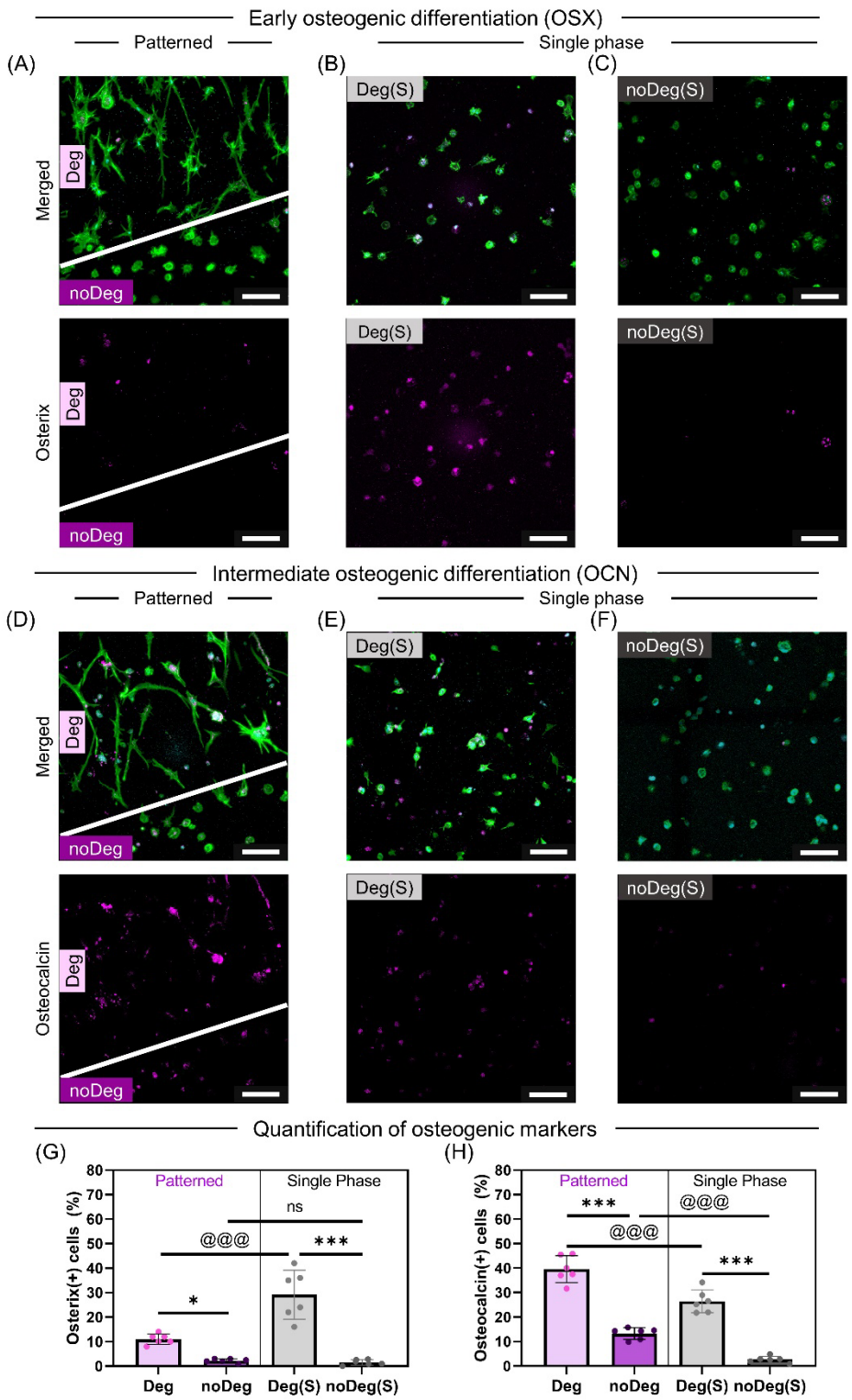

454

455 ***Figure 5: Osteogenic and adipogenic differentiation of encapsulated hMSCs in patterned***

456 ***materials on day 14.*** *Actin (Phalloidin/green) and nucleus (SYTOX/cyan) staining with Osterix*

457 *(OSX, magenta, A-C) or Osteocalcin (OCN, magenta, D-F). Comparison between patterned*
458 *materials (A, D), single-phase Deg(S) (B, E) and single-phase noDeg(S) (C, F), quantified in bar*
459 *plots (G, H), which show the mean and standard deviation of n = 6 fields of view containing multiple*
460 *cells (n ≥ 150 cells per phase and condition). Statistical significance with ANOVA and Bonferroni*
461 *correction. Scale bar: 100 µm.*

462 The anisotropic biophysical cues provided by the patterned materials already induced significantly
463 enhanced and spatially segregated osteogenic differentiation of hMSC over 14 days in growth media
464 (Fig. 5). The early osteogenic marker OSX (Fig 5A-C) was expressed in the Deg single-phase
465 materials (Fig. 5B) and also in the Deg phase of patterned materials (Fig. 5A), though to a lower
466 extent (Fig. 5G). Furthermore, the intermediate osteogenic marker OCN, indicative of further
467 differentiated hMSCs, was significantly higher (Fig. 5H) in the Deg sections of patterned materials
468 (Fig 5D) compared to single-phase Deg materials (Fig. 5E). The noDeg phases in both patterned and
469 single-phase materials (Fig. 5C, F) did not allow osteogenic differentiation of hMSCs.

470 With flow cytometry, individual cells can be explored on a higher parametric level. Cells were
471 retrieved from three different types of hydrogels: single-phase degradable (Deg(S)), single-phase
472 non-degradable (noDeg(S)), and patterned 3D hydrogels (patterned), after culturing for 14 days. We
473 investigated the changes in cell phenotype by analyzing various cell surface markers, as well as
474 intracellular markers, allowing to trace the differentiation from stem-like characteristics towards
475 osteogenic cells (Fig. 6). Dimension reduction (UMAP) of all cells from the three groups showed
476 distinct clustering of the groups (Fig 6A-G). The mean fluorescence intensity (geometric MFI)
477 allowed to determine the expression level of measured markers. All retrieved cells from the 3D
478 materials were negative for the markers CD45, CD34, CD166, CD271 and CD146. The surface
479 markers CD90, CD105, CD73, considered as minimal criteria for hMSC, showed altered positive

480 expression levels with CD90 (Fig 6H), especially, being higher expressed in the degradable
481 compared to the noDeg material (Fig 6H, K).

482 The intracellular markers Osteocalcin (OCN), Alkaline Phosphatase (ALP) and Osteopontin (OPN)
483 allowed to trace the osteogenic differentiation of encapsulated hMSCs, which show an increased z-
484 score of OCN and ALP in Deg materials (Fig. 6I, K). Interestingly, a small subset of cells in the
485 noDeg material expressed higher levels of OPN (Fig 6J, K).

486 To evaluate the difference between the patterned and single-phase materials, a principal component
487 analysis was performed (Fig 6L). The *x-axis* represents Principal Component 1 (PC1), which
488 explains 45.3% of the variance, while the *y-axis* represents Principal Component 2 (PC2), capturing
489 18.7% of the variance. Despite the overlap between the groups, the trend shows 3 distinct groups
490 enclosed in a 90% CI ellipse with an overall 64% explained variances. This indicates that the
491 patterned material induced a distinct cellular composition that differs from the respective single-
492 phase materials.

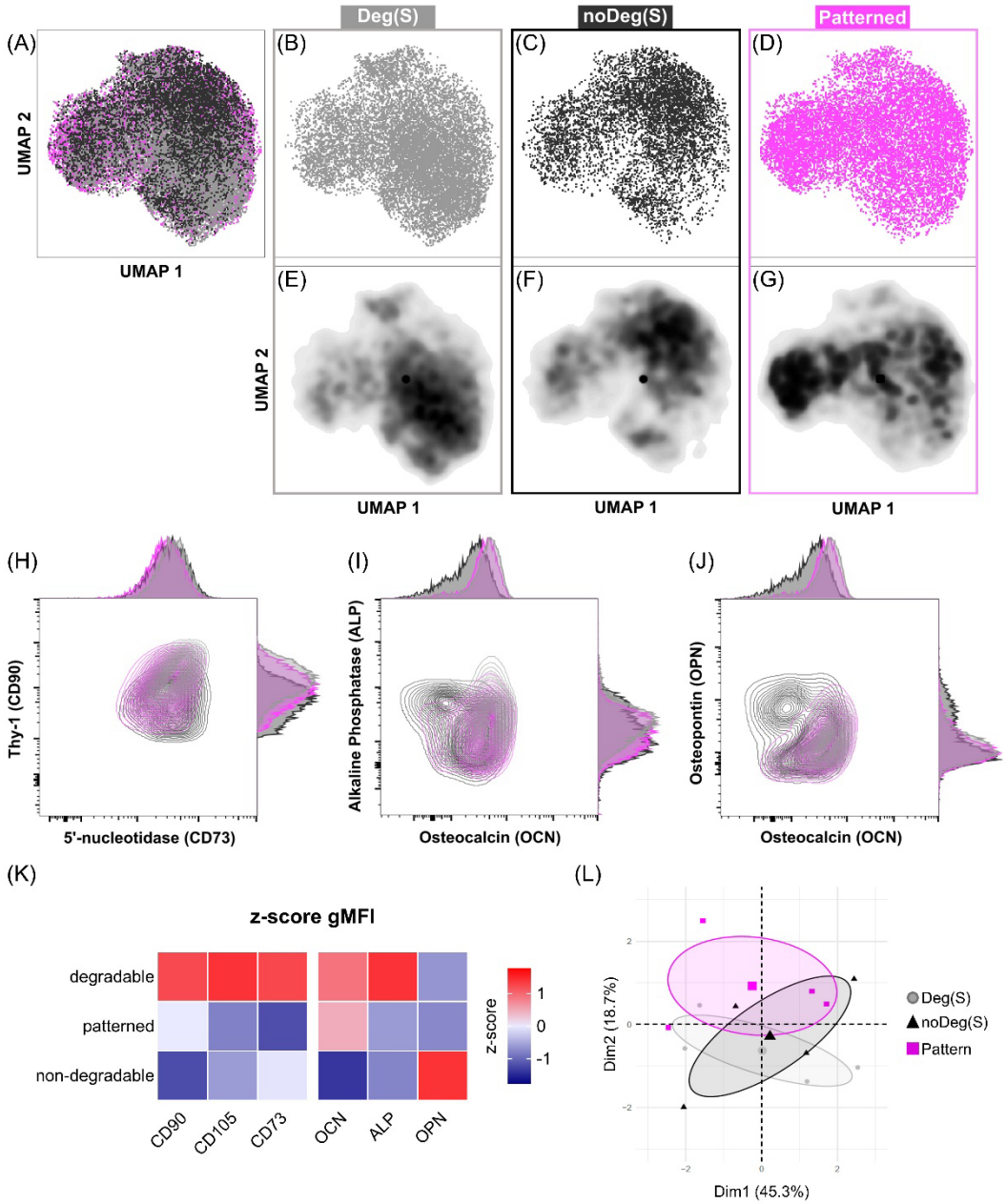

Figure 6: Flow cytometry evaluation of hMSCs retrieved from 3D patterned and single-phase materials after culturing for 14 days. *UMAPs cluster plots merged (A), Deg(S) (B), noDeg(S) (C) and patterned (D), and the corresponding density plots of Deg(S) (E), noDeg(S) (F) and pattered (G). Multiplots, contour plots plus histograms of the expression of: CD73 vs. CD90 (H), OCN vs. ALP (I) and OCN vs. OPN (J). z-score quantification of hMSCs minimal criteria markers (CD105, CD73, CD90) and differentiation markers (OCN, ALP, OPN) (K). Principal component analysis for*

500 *dimension 1 (Dim 1, 45,3 %) and dimension 2 (Dim 2, 18,7 %), the big symbols show the center of*
501 *the ellipse and the smaller symbols the different batches (L). n=4 batches containing 1x10^5 cells, for*
502 *each material.*

503 **3.4 Enhanced and spatially guided mechanosensing via YAP/TAZ signaling in 3D patterned**
504 **materials compared to single-phase counterparts**

505 After establishing the significant differences in patterned hMSC projected cell area, circularity,
506 collective cell alignment and osteogenic differentiation, we investigated the underlying mechanism.
507 Based on the observation of morphological changes and associated cytoskeletal tension in degradable
508 regions, we investigated YAP positive expression (YAP(+)) and nuclear to cytoplasmic localization
509 within single cells in patterned materials (Fig. 7A-C) and compared it to the single-phase
510 counterparts (Fig 6D-G).

511 The fraction of YAP(+) cells was significantly higher in Deg materials patterned (Fig 7A) and single-
512 phase (Fig 7D) compared to noDeg (Fig. 7E) on day 14 (Fig 7H). Independent of the material or the
513 patterning, the YAP expression was equally distributed over the nucleus and the cytoplasm on day 1
514 (Fig 7I). On day 14, there was a nuclear translocation (nuc./cyto. >1) in Deg materials, patterned (Fig
515 7B) and single-phase Deg (Fig 7F), whereas for the noDeg materials, in patterned (Fig 7C) and in
516 single-phase (Fig 7G), it remained close to 1. The effect of nuclear YAP translocation was
517 significantly higher in Deg phases of patterned materials compared to Deg phases in single-phase
518 materials (Fig. 7I).

519 To test the influence of degradation in the YAP translocation, the MMPsens peptide crosslinker was
520 replaced with the homologous non-degradable scramble peptide (MMPscr). The MMPscr allowed the
521 comparison of the degradable and non-degradable material with the same chemical crosslinking and
522 mechanical properties (ex. crosslinker length). The MMPscr patterned materials showed a very

523 similar behavior on day 1 (data not shown) compared to day 14 (Fig. 7J-L). The lack of degradation
524 in the MMPscr regions led to a rounded cell morphology with a similar YAP expression (Fig. 7J-K)
525 as the one seen in noDeg phases (Fig. 7G). Both phases with MMPscr and noDeg patterned materials
526 had a similar YAP (+) cell percentage (Fig. 7M) and YAP localization (Fig. 7N), with no significant
527 differences neither between phases nor over time.

528 To test the relevance of integrin activation and cell-matrix interaction with alginate, we used
529 materials lacking RGD adhesion peptides (Fig. 7O-S). The cells in noRGD patterned materials
530 showed a similar behavior in the two phases on day 1 (data not shown) as well as on day14 (Fig 7O-
531 Q). The fraction of YAP(+) cells was lower (Fig. 7R) compared to materials with RGD (Fig. 7H).
532 Moreover, there were no significant differences in YAP(+) cells (Fig 7R) or localization (Fig. 7S),
533 neither between phases nor over time.

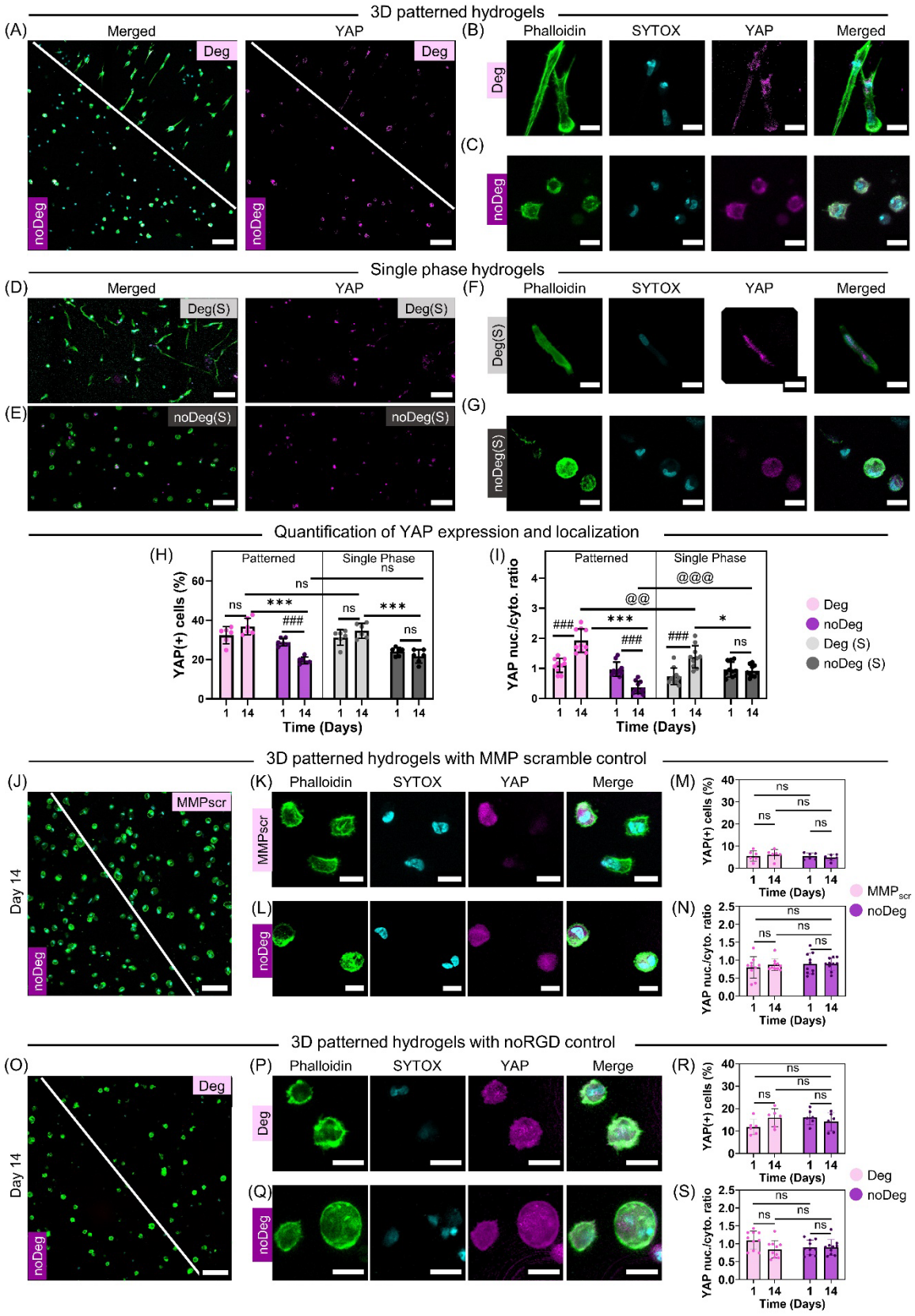
3D patterned hydrogels
(A)
Merged
YAP
Deg
noDeg
(B)
Phalloidin
SYTOX
YAP
Merged
(C)
Single phase hydrogels
(D)
Deg(S)
(E)
noDeg(S)
(F)
(G)
Quantification of YAP expression and localization
(H)
Patterned
Single Phase
YAP(+) cells (%)
Time (Days)
(I)
YAP nuc./cyto. ratio
Deg
noDeg
Deg (S)
noDeg (S)
3D patterned hydrogels with MMP scramble control
(J)
MMPscr
Day 14
(K)
(L)
(M)
(N)
MMP$_{scr}$
3D patterned hydrogels with noRGD control
(O)
(P)
(Q)
(R)
(S)

534

535 ***Figure 7: YAP expression and nuclear to cytoplasmic localization of encapsulated hMSCs in***
536 ***patterned materials vs. single-phase materials, and controls with MMP scramble peptide and***
537 ***without RGD on day 14.*** *hMSC staining with actin (Phalloidin/green), nucleus (SYTOX/cyan) and*
538 *YAP expression (magenta). YAP expression in patterned materials: overview (A), representative*
539 *single cell images in the Deg (B) and noDeg (C) phase. YAP expression in single-phase materials:*
540 *overview of Deg (D) and noDeg (E) and representative single cells in Deg (F) and noDeg (G)*
541 *materials. Comparison between patterned and single-phase materials of YAP expression (H) and*
542 *nuclear to cytoplasmic localization (I). YAP expression in patterned materials with MMPscr control:*
543 *overview (J) and representative single cell images in Deg (K) and noDeg (L) regions. Quantification*
544 *of YAP expression (M) and YAP localization (N) in MMPscr materials. YAP expression in patterned*
545 *materials with noRGD control: overview (O) and representative single cell images in Deg (P) and*
546 *noDeg (Q) regions. Quantification of YAP expression (R) and YAP localization (S) in noRGD*
547 *materials. Bar plots show the mean and standard deviation of n = 6 fields of view containing*
548 *n>120cells (H, M, R) and of n = 10 representative single cells from Deg vs. noDeg regions (I, N, S).*
549 *Statistical significance with ANOVA and Bonferroni correction. Scale bar: 100 µm (A, D, E, J, O)*
550 *and 20 µm (B, C, F, G, K, L, P, Q).*

551

552 **3.5 Additional biochemical stimuli can enhance the spatially guided hMSC osteogenic**
553 **differentiation**

554 hMSC differentiation was further tested under osteogenic media to evaluate the effect of biochemical
555 stimuli in patterned materials. Cell morphology patterns are enhanced with osteogenic media (Fig.
556 8A-E) when compared to growth media (Fig. 3A), showing larger projected cell area (Fig. 8B) and
557 elongated cells with lower circularity (Fig. 8C) in Deg regions.

558 The intermediate osteogenic marker OCN had higher expression in osteogenic media (Fig. 8F)
559 compared to growth media and shows a significantly higher expression in Deg phases compared to
560 noDeg phases (Fig. 8F, K). Despite the biochemical stimuli of osteogenic media, the restrictive
561 environment of noDeg sections resulted in only a low number of OCN positive cells (Fig 8K). The
562 late osteogenic marker (mineralization, OsteoImage) (Fig. 8G, L) also had higher expression in
563 osteogenic media compared to growth media, with significantly higher mineralized area in Deg
564 sections compared to noDeg sections (Fig. 8L).

565 The fraction of YAP(+) cells in osteogenic media (Fig. 8H) showed also increased expression on day
566 14 in the Deg regions, but with overall increased values compared to growth media (Fig. 5M). The
567 YAP nuclear to cytoplasmic ratio shows a similar significant pattern over time in osteogenic media
568 compared to growth media (Fig. 8N), with nuclear translocation in the Deg phase (Fig. 8I) and
569 cytoplasmic expression in the noDeg phase (Fig. 8J). In the Deg phase the use of osteogenic media
570 significantly enhanced the nuclear translocation compared to growth media (Fig. 8M, N).

571

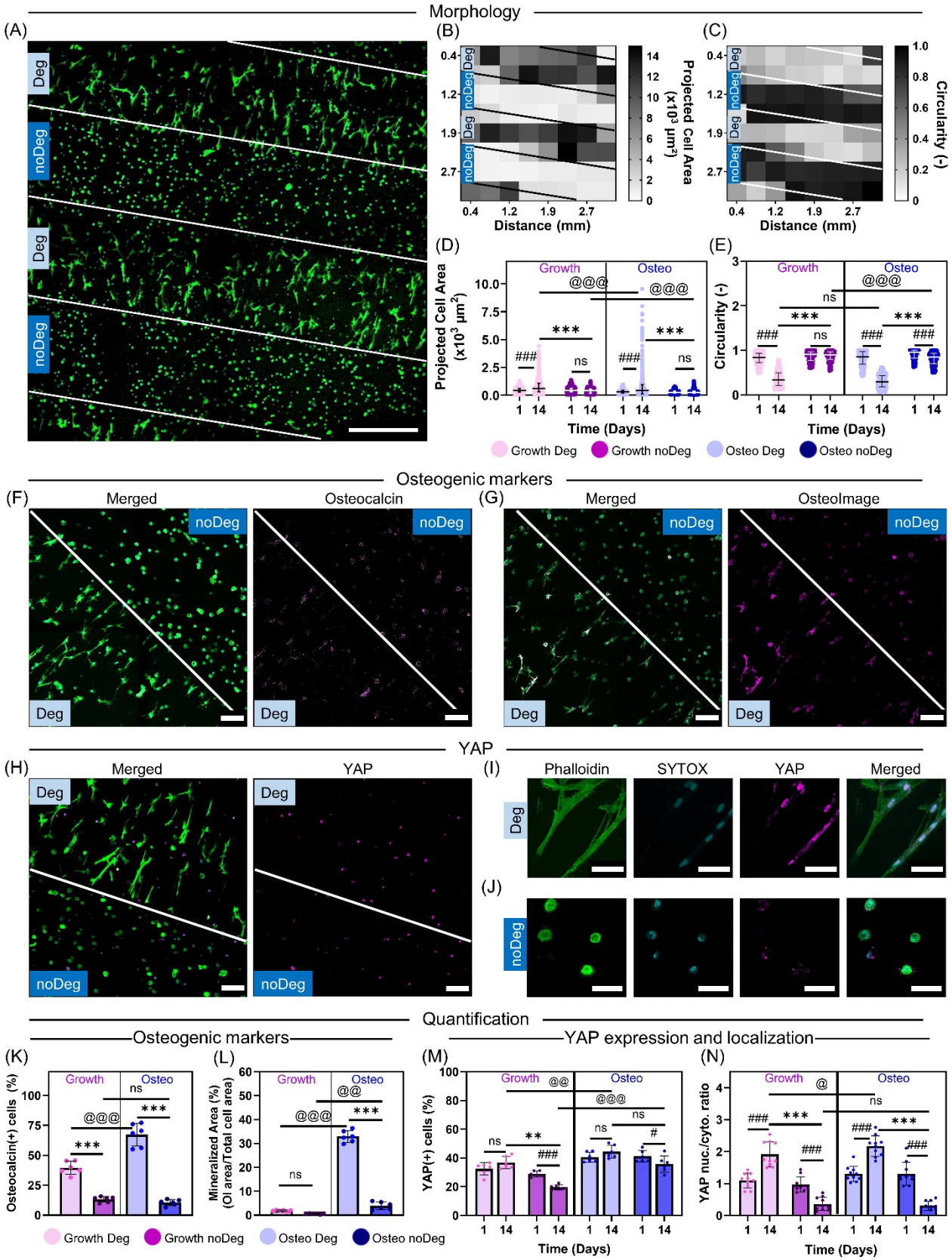
Morphology
(A)
Deg
noDeg
Deg
noDeg
(B)
Projected Cell Area (x10³ µm²)
Distance (mm)
(C)
Circularity (-)
Distance (mm)
(D)
Projected Cell Area (x10³ µm²)
Growth
Osteo
Time (Days)
(E)
Circularity (-)
Growth
Osteo
Time (Days)
Growth Deg
Growth noDeg
Osteo Deg
Osteo noDeg
Osteogenic markers
(F)
Merged
Osteocalcin
(G)
Merged
OsteoImage
YAP
(H)
Merged
YAP
(I)
Phalloidin
SYTOX
YAP
Merged
(J)
Quantification
Osteogenic markers
YAP expression and localization
(K)
Osteocalcin(+) cells (%)
(L)
Mineralized Area (%) (OI area/Total cell area)
(M)
YAP(+) cells (%)
Time (Days)
(N)
YAP nuc./cyto. ratio
Time (Days)
Growth Deg
Growth noDeg
Osteo Deg
Osteo noDeg

572

573 ***Figure 8: Enhanced cell response in patterned materials by osteogenic media on day 14.***
574 *Representative actin (Phalloidin/green) and nucleus (SYTOX/cyan) staining of patterned materials*
575 *with hMSCs in osteogenic media (A). Heatmap quantification with an 8x8 grid of projected cell area*
576 *(B) and cell circularity (C). Dot graph of growth vs osteogenic media of cells in patterned materials*
577 *(> 400 single cells per phase and condition) of projected cell area (D) and circularity (E) on day 14*
578 *(see Suppl. Fig. S3D-F for corresponding images and heat maps on day 1). Representative*
579 *Osteocalcin (magenta, F) or osterix (magenta, G) staining and expression quantification of OCN (K)*
580 *and mineralization (L). Representative YAP staining overview (H) and single cells from Deg (I) and*
581 *noDeg(J) sections. Quantification fraction of YAP(+) cells (M) and YAP localization (N). Dot graphs*
582 *show statistical significance with Kruskal-Wallis and Dunn's correction and bar plots evaluated with*
583 *statistical significance with ANOVA and Bonferroni correction. Scale bar: 500 µm (A), 250µm (F, G,*
584 *H) and 20 µm (I, J).*

585 **4 Discussion**

586 Degradation patterned materials enhance encapsulated hMSC spread morphology, allow collective
587 cell alignment, stimulate mechanotransduction and promote osteogenic differentiation, when
588 compared to single phase materials. By investigating patterned hydrogels as opposed to equivalent
589 single-phase matrices, we aimed to highlight the importance of using multicompartment materials in
590 biomaterial design. In addition, the patterned materials with anisotropic hydrogel degradation
591 allowed elucidating the role of degradation, without additional biophysical (such as stiffness) or
592 biochemical (such as osteogenic media) cues. Our findings offer insights into how these anisotropic
593 materials influence cell response, potentially leading to better strategies mimicking tissue anisotropy,
594 with applications in biofabrication and tissue engineering.

595 The anisotropic alginate-based hydrogels used in this research consist of two soft (<3kPa) 3D
596 microenvironments for cells, with comparable initial elastic modulus at day 1, and emerging patterns

597 through degradation over time. The comparable initial elastic modulus of both phases allows a direct
598 comparison on degradability effects, excluding other biophysical properties (i.e. matrix stiffness),
599 which have already been studied [44][24]. Moreover, the combination of both matrices in a patterned
600 multicomponent material results in a structural advantage over time, as the single phase Deg
601 materials crumble and start disintegrating due to degradation, while patterned materials keep their
602 shape after 14 days (Suppl. Fig. S5). It is important to highlight the tuneability of the matrix platform
603 used, which allows different combinations of mechanical and degradation properties (Fig. 1F-G).
604 Interestingly, the click reaction described in Fig. 1G shows a maximum elastic modulus at N:T ratio
605 0.5. This is consistent with the description of an unexpected dimer formation, following a 1:2 (N:T)
606 stoichiometry [45].

607 Cell spreading is dependent on the matrix degradation and this is enhanced in Deg sections of
608 patterned materials compared to single phase counterparts. Changes in morphology are a result of the
609 remodeling of the immediate environment [30] and consistently described in MMP-sensitive peptide
610 crosslinked materials [46]. Our research showed that the interphases of the patterned materials not
611 only lead to spatially segregated cell morphology, but also influence the collective cell alignment
612 perpendicular to the stripe main axis. Cell alignment in patterned materials has been previously
613 described on 2D topographical directed patterns [47][48][49] and in 2D mesh scaffolds [50],
614 exhibiting a parallel alignment to the groves/ridges, or perpendicular to them in wider curvatures
615 (>1000 μm) [51]. However, less is known about the mechanism for collective cell alignment within
616 3D matrices. Previous studies report the perpendicular cell alignment to be a result of force and
617 neighboring tensile stress [52]. Our research showed that cell alignment is dependent on the stripe
618 dimensions (Fig 4, broader stripes show no alignment), patterning (Suppl. Fig S4, single phase
619 hydrogels show no collective alignment) and, probably, on the material´s differential swelling
620 properties (Suppl. Fig S4, constrained swelling show no alignment). The direct transfer of

621 mechanisms of collective cell alignment into 3D matrices is still at early stage, as 3D environments
622 offer multiple factors that can influence cell, such as mechanical properties, adhesive ligand
623 concentration, crosslink type and density. Yet, understanding and guiding collective cell alignment
624 will be important for developing functional biomaterials that mimic biological anisotropic tissues,
625 which rely on fiber/cell directionality for optimal performance [53].

626 The 3D patterns in hydrogel degradation allowed spatially guided hMSC differentiation, promoting
627 enhanced osteogenic differentiation in the Deg region compared to the noDeg, or single-phase
628 degradable materials in growth media (Fig. 5). Strikingly, an early osteogenesis stage as shown by
629 OSX expression could be promoted solely by biophysical factors after 14 day culture in growth
630 media (hMSCs in Deg single-phase materials, Fig. 5B). This effect was enhanced in patterned
631 materials, which at the same time point showed OCN expression, an intermediate osteogenic marker
632 (Fig 5D). Our findings agree with previous studies on stiffness-degradation 3D patterned materials
633 showing that soft and Deg matrices foster osteogenesis [24]. Our study highlights the importance of
634 matrix degradability for osteogenesis, and the potential of using patterned materials for enhancing
635 and guiding osteogenic differentiation.

636 Moreover, biochemical factors (osteogenic media) in combination with patterned materials, enabled
637 late osteogenesis and mineralization in Deg phases. Notably, mineralization within the Deg phases
638 was only observed under osteogenic media, consistent with studies showing that biomineralization is
639 a complex process [54]. Despite the biochemical cues from osteogenic media were available for cells
640 in both Deg and noDeg phases of the patterned material, the guidance of the patterns is evident with
641 broader cell spreading, higher osteogenic differentiation and increased YAP nuclear translocation in
642 the Deg phases compared to the noDeg regions. These findings highlight the interplay between
643 biochemical and biophysical cues modulating cell behavior and the synergistic effect by anisotropic
644 patterned hydrogels.

645 Further flow cytometry analysis of hMSCs encapsulated in hydrogels enabled us to identify changes
646 in cell phenotype between the materials. The density plots showed clearly distinct clustering behavior
647 of the Deg and noDeg single-phase materials (Fig 6B, C), however the patterned material did not
648 cluster along the two single-phase materials (Fig 6D, G), hinting towards distinct processes in
649 anisotropic materials and not only replicating the two individual isotropic materials. All cells were
650 consistent with the minimal criteria markers: negative for CD45, CD34, , and positive for CD90,
651 CD73, CD105 [55]. There were no hMSCs subpopulations identified as the cells were negative for
652 CD166, CD271 and CD146 [56]. Deg materials led to the upregulation of CD90 (Fig. 6H), which
653 controls vital cellular processes, including cell–cell and cell–matrix interactions, cell adhesion and
654 cell response to dynamic matrices [57][58]. Notably, CD73 shows a downregulation in the patterned
655 materials when compared to Deg and noDeg. This effect could be due to the additional mechanical
656 strain from the anisotropic material interfaces, as previous studies have shown that CD73 is
657 downregulated in mechanically loaded cells [59].

658 The intracellular markers Osteocalcin (OCN), Alkaline Phosphatase (ALP) and Osteopontin (OPN)
659 allowed to trace the osteogenic differentiation of encapsulated hMSCs. In accordance with the
660 immunofluorescence staining for Osteocalcin (Fig 5), Deg and patterned materials induced
661 osteogenic differentiation in the encapsulated cells, as shown by the increased OCN expression (Fig
662 6 I, J) compared to noDeg. It is important to highlight that the patterned materials were analyzed as a
663 bulk (Deg+noDeg regions), therefore the enhanced effects in patterned Deg phase were not captured
664 using this method. This is a limitation of bulk analyses using flow cytometry, as opposed to image-
665 based methods and immunofluorescence.

666 Interestingly a small subset of cells in the noDeg material expressed higher levels of OPN (Fig 6 J).
667 OPN is a multifunctional protein, which has a role in inflammatory processes [60]. Non-degradable

668 alginate-based matrices have been previously reported to upregulate differentially expressed genes
669 involved in inflammatory response in breast cancer cells [61].

670 YAP nuclear translocation and mechanotransduction is enhanced in Deg sections of patterned
671 materials. In line with previous studies, Deg materials showed a higher YAP nuclear translocation
672 compared to noDeg, triggered solely by the degradation of the material [31][30][62]. Our research
673 takes this effect further by evaluating the enhanced mechanotransduction effect in patterned materials
674 compared to single-phase counterparts (Fig 7A-I). The enhanced hMSCs spreading and collective
675 cell alignment resulting from the anisotropic material interphases, seem to enhance
676 mechanosensation by YAP nuclear translocation. As underlying mechanism, we identify two key
677 factors: matrix degradation (as no YAP nuclear translocation was observed in MMPscr materials,
678 Fig. 7J-N) and the need of cell-matrix adhesion via integrin activation (as no YAP nuclear
679 translocation was observed in noRGD materials, Fig. 7O-S). This ultimately leads to enhanced
680 mechanotransduction and osteogenic differentiation in anisotropic hydrogels.

681 **5 Conclusions**

682 In summary, we show that anisotropic hydrogel degradation enhances hMSC cell spreading in 3D,
683 collective cell alignment, mechanotransduction and osteogenic differentiation, compared to the
684 single-phase equivalents. Patterned material´s interphase proximity, matrix-bound cell adhesion
685 peptide RGD and degradable crosslinking peptides are required for patterned mechanosensing. These
686 combined results highlight the importance of developing 3D patterned biomaterials to mimic the
687 anisotropy in biological tissues, for both fundamental understanding of guided collective cell
688 behavior and tissue anisotropy, as well as for applications in biofabrication and tissue engineering.

689 **6 Acknowledgements**

The authors acknowledge the support from all group members of Cipitria, Schmidt-Bleek and Duda's laboratories. We thank the Cell Core Facility of Charité-Universitätsmedizin for providing the cells used in this study. In addition, we thank the Research Workshop at the Charité-Universitätsmedizin Berlin for developing and manufacturing some experimental devices. We thank Andreas Engels for printing the photomasks used in this research. We thank Mario Thiele from Charité-Universitätsmedizin and Samik Real from Hasso Plattner-Institute for contributing with the macros used in this research. In addition to the support given by Ansgar Petersen and Erik Brauer from JWI.

7 CRediT authorship contribution statement

A Cipitria conceived the idea. CA Garrido, A Cipitria developed the methodology. CA Garrido, DS Garske performed the experiments. CH Bucher performed the flow cytometry experiments and data analysis. S Amini supported the micro indentation experiments. CA Garrido quantified and analyzed the data. CA Garrido and A Cipitria drafted the manuscript. DS Garske contributed with the visualization of the data. A Cipitria, K Schmidt-Bleek and GN Duda supervised, reviewed and edited the original data and manuscript. All authors discussed the results and contributed to the final manuscript.

8 Declaration of competing interest

The authors declare that the research was conducted in the absence of any commercial or financial relationships that could be considered as a potential conflict of interest.

9 Funding

This work was funded by the Deutsche Forschungsgemeinschaft (DFG) Collaborative Research Center (CRC) 1444 grant (C.A.G, D.S.G.). A. Cipitria also acknowledges the funding from the DFG Emmy Noether grant (CI 203/2-1), IKERBASQUE Basque Foundation for Science, and from the

Spanish Ministry of Science and Innovation, grant PID2021-123013OB-I00 funded by MCIN/AEI/10.13039/501100011033/FEDER, UE.

10 Data and code availability

All raw and processed data are available in the publicly accessible Edmond repository of the Max Planck Society: https://doi.org/10.17617/3.WLTITB

11 References

[1] M. Krampera, K. Le Blanc, Mesenchymal stromal cells: Putative microenvironmental modulators become cell therapy, Cell Stem Cell 28 (2021) 1708–1725. https://doi.org/10.1016/j.stem.2021.09.006.

[2] A.C. Wilkinson, K.J. Igarashi, H. Nakauchi, Haematopoietic stem cell self-renewal in vivo and ex vivo, Nat. Rev. Genet. 21 (2020) 541–554. https://doi.org/10.1038/s41576-020-0241-0.

[3] H.S. Kim, S.G. Kumbar, S.P. Nukavarapu, Biomaterial-directed cell behavior for tissue engineering, Curr. Opin. Biomed. Eng. 17 (2021) 100260. https://doi.org/10.1016/j.cobme.2020.100260.

[4] C.A. Deforest, K.S. Anseth, Advances in bioactive hydrogels to probe and direct cell fate, Annu. Rev. Chem. Biomol. Eng. 3 (2012) 421–444. https://doi.org/10.1146/annurev-chembioeng-062011-080945.

[5] E.C. González-Díaz, S. Varghese, Hydrogels as extracellular matrix analogs, Gels 2 (2016). https://doi.org/10.3390/gels2030020.

[6] A.M. Kloxin, C.J. Kloxin, C.N. Bowman, K.S. Anseth, Mechanical properties of cellularly responsive hydrogels and their experimental determination, Adv. Mater. 22 (2010) 3484–3494. https://doi.org/10.1002/adma.200904179.

[7] M. Guvendiren, J.A. Burdick, Engineering synthetic hydrogel microenvironments to instruct stem cells, Curr. Opin. Biotechnol. 24 (2013) 841–846. https://doi.org/10.1016/j.copbio.2013.03.009.

[8] L.R. Smith, S. Cho, D.E. Discher, Stem cell differentiation is regulated by extracellular matrix mechanics, Physiology 33 (2018) 16–25. https://doi.org/10.1152/physiol.00026.2017.

[9] C. Branco da Cunha, D.D. Klumpers, W.A. Li, S.T. Koshy, J.C. Weaver, O. Chaudhuri, P.L. Granja, D.J. Mooney, Influence of the stiffness of three-dimensional alginate/collagen-I interpenetrating networks on fibroblast biology, Biomaterials 35 (2014) 8927–8936. https://doi.org/10.1016/j.biomaterials.2014.06.047.

[10] N. Huebsch, E. Lippens, K. Lee, M. Mehta, S.T. Koshy, M.C. Darnell, R.M. Desai, C.M. Madl, M. Xu, X. Zhao, O. Chaudhuri, C. Verbeke, W.S. Kim, K. Alim, A. Mammoto, D.E. Ingber, G.N. Duda, D.J. Mooney, Matrix elasticity of void-forming hydrogels controls transplanted-stem-cell-mediated bone formation, Nat. Mater. 14 (2015) 1269–1277. https://doi.org/10.1038/nmat4407.

[11] O. Chaudhuri, L. Gu, D. Klumpers, M. Darnell, S.A. Bencherif, J.C. Weaver, N. Huebsch, H. Lee, E. Lippens, G.N. Duda, D.J. Mooney, Hydrogels with tunable stress relaxation regulate stem cell fate and activity, Nat. Mater. 15 (2016) 326–334. https://doi.org/10.1038/nmat4489.

[12] O. Chaudhuri, J. Cooper-White, P.A. Janmey, D.J. Mooney, V.B. Shenoy, Effects of extracellular matrix viscoelasticity on cellular behaviour, Nature 584 (2020) 535–546. https://doi.org/10.1038/s41586-020-2612-2.

[13] S. Khetan, M. Guvendiren, W.R. Legant, D.M. Cohen, C.S. Chen, J.A. Burdick, Degradation-mediated cellular traction directs stem cell fate in covalently crosslinked three-dimensional hydrogels, Nat. Mater. 12 (2013) 458–465. https://doi.org/10.1038/nmat3586.

[14] V. V. Rao, M.E. Wechsler, E. Cravens, S.J. Wojda, A.S. Caldwell, B.E. Kirkpatrick, S.W. Donahue, K.S. Anseth, Granular PEG hydrogels mediate osteoporotic MSC clustering via N-cadherin influencing the pro-resorptive bias of their secretory profile, Acta Biomater. 145 (2022) 77–87. https://doi.org/10.1016/j.actbio.2022.04.023.

[15] M.D. Davidson, E. Ban, A.C.M. Schoonen, M.H. Lee, M. D'Este, V.B. Shenoy, J.A. Burdick, Mechanochemical Adhesion and Plasticity in Multifiber Hydrogel Networks, Adv. Mater. 32 (2020) 1–8. https://doi.org/10.1002/adma.201905719.

[16] A. Sanchez-Rubio, V. Jayawarna, E. Maxwell, M.J. Dalby, M. Salmeron-Sanchez, Keeping It Organized: Multicompartment Constructs to Mimic Tissue Heterogeneity, Adv. Healthc. Mater. (2023) 2202110. https://doi.org/10.1002/adhm.202202110.

[17] N. Broguiere, I. Lüchtefeld, L. Trachsel, D. Mazunin, R. Rizzo, J.W. Bode, M.P. Lutolf, M. Zenobi-Wong, Morphogenesis Guided by 3D Patterning of Growth Factors in Biological Matrices, Adv. Mater. 32 (2020) 1–10. https://doi.org/10.1002/adma.201908299.

[18] C.A. DeForest, K.S. Anseth, Cytocompatible click-based hydrogels with dynamically tunable properties through orthogonal photoconjugation and photocleavage reactions, Nat. Chem. 3 (2011) 925–931. https://doi.org/10.1038/nchem.1174.

[19] K.H. Song, C.B. Highley, A. Rouff, J.A. Burdick, Complex 3D-Printed Microchannels within Cell-Degradable Hydrogels, Adv. Funct. Mater. 28 (2018) 1–10. https://doi.org/10.1002/adfm.201801331.

[20] A. Thomas, I. Orellano, T. Lam, B. Noichl, M.A. Geiger, A.K. Amler, A.E. Kreuder, C. Palmer, G. Duda, R. Lauster, L. Kloke, Vascular bioprinting with enzymatically degradable bioinks via multi-material projection-based stereolithography, Acta Biomater. 117 (2020) 121–132. https://doi.org/10.1016/J.ACTBIO.2020.09.033.

[21] D. Hanjaya-Putra, K.T. Wong, K. Hirotsu, S. Khetan, J.A. Burdick, S. Gerecht, Spatial control of cell-mediated degradation to regulate vasculogenesis and angiogenesis in hyaluronan hydrogels, Biomaterials 33 (2012) 6123–6131. https://doi.org/10.1016/j.biomaterials.2012.05.027.

[22] B. Trappmann, B.M. Baker, W.J. Polacheck, C.K. Choi, J.A. Burdick, C.S. Chen, Matrix degradability controls multicellularity of 3D cell migration, Nat. Commun. 8 (2017) 371. https://doi.org/10.1038/s41467-017-00418-6.

[23] C.A. Garrido, D.S. Garske, M. Thiele, S. Amini, S. Real, G.N. Duda, K. Schmidt-Bleek, A. Cipitria, Hydrogels with stiffness-degradation spatial patterns control anisotropic 3D cell response, Biomater. Adv. 151 (2023) 2023.01.25.525504. https://doi.org/10.1016/j.bioadv.2023.213423.

[24] S. Khetan, J.A. Burdick, Patterning network structure to spatially control cellular remodeling and stem cell fate within 3-dimensional hydrogels, Biomaterials 31 (2010) 8228–8234. https://doi.org/10.1016/j.biomaterials.2010.07.035.

[25] L.G. Vincent, A.J. Engler, Stem cell differentiation: Post-degradation forces kick in, Nat. Mater. 12

(2013) 384–386. https://doi.org/10.1038/nmat3636.

[26] A. Lueckgen, D.S. Garske, A. Ellinghaus, D.J. Mooney, G.N. Duda, A. Cipitria, Enzymatically-degradable alginate hydrogels promote cell spreading and in vivo tissue infiltration, Biomaterials 217 (2019) 119294. https://doi.org/10.1016/j.biomaterials.2019.119294.

[27] S. Khetan, M. Guvendiren, W.R. Legant, D.M. Cohen, C.S. Chen, J.A. Burdick, Degradation-mediated cellular traction directs stem cell fate in covalently crosslinked three-dimensional hydrogels, Nat. Mater. 12 (2013) 458–465. https://doi.org/10.1038/nmat3586.

[28] S. Dupont, L. Morsut, M. Aragona, E. Enzo, S. Giulitti, M. Cordenonsi, F. Zanconato, J. Le Digabel, M. Forcato, S. Bicciato, N. Elvassore, S. Piccolo, Role of YAP/TAZ in mechanotransduction, Nature 474 (2011) 179–183. https://doi.org/10.1038/nature10137.

[29] A. Saraswathibhatla, D. Indana, O. Chaudhuri, Cell–extracellular matrix mechanotransduction in 3D, Nat. Rev. Mol. Cell Biol. (2023) 1–22. https://doi.org/10.1038/s41580-023-00583-1.

[30] S.R. Caliari, S.L. Vega, M. Kwon, E.M. Soulas, J.A. Burdick, Dimensionality and spreading influence MSC YAP/TAZ signaling in hydrogel environments, Biomaterials 103 (2016) 314–323. https://doi.org/10.1016/j.biomaterials.2016.06.061.

[31] N. Gjorevski, N. Sachs, A. Manfrin, S. Giger, M.E. Bragina, P. Ordóñez-Morán, H. Clevers, M.P. Lutolf, Designer matrices for intestinal stem cell and organoid culture, Nature 539 (2016) 560–564. https://doi.org/10.1038/nature20168.

[32] X. Cai, K.C. Wang, Z. Meng, Mechanoregulation of YAP and TAZ in Cellular Homeostasis and Disease Progression, Front. Cell Dev. Biol. 9 (2021) 1–12. https://doi.org/10.3389/fcell.2021.673599.

[33] N. Gjorevski, M. Nikolaev, T.E. Brown, O. Mitrofanova, N. Brandenberg, F.W. DelRio, F.M. Yavitt, P. Liberali, K.S. Anseth, M.P. Lutolf, Tissue geometry drives deterministic organoid patterning, Science (80-.). 375 (2022). https://doi.org/10.1126/science.aaw9021.

[34] S. Reinke, S. Geissler, W.R. Taylor, K. Schmidt-Bleek, K. Juelke, V. Schwachmeyer, M. Dahne, T. Hartwig, L. Akyüz, C. Meisel, N. Unterwalder, N.B. Singh, P. Reinke, N.P. Haas, H.-D. Volk, G.N. Duda, Terminally Differentiated CD8 + T Cells Negatively Affect Bone Regeneration in Humans, Sci. Transl. Med. 5 (2013) 177ra36-177ra36. https://doi.org/10.1126/scitranslmed.3004754.

[35] A. Andrzejewska, R. Catar, J. Schoon, T.H. Qazi, F.A. Sass, D. Jacobi, A. Blankenstein, S. Reinke, D. Krüger, M. Streitz, S. Schlickeiser, S. Richter, N. Souidi, C. Beez, J. Kamhieh-Milz, U. Krüger, T. Zemojtel, K. Jürchott, D. Strunk, P. Reinke, G. Duda, G. Moll, S. Geissler, Multi-Parameter Analysis of Biobanked Human Bone Marrow Stromal Cells Shows Little Influence for Donor Age and Mild Comorbidities on Phenotypic and Functional Properties, Front. Immunol. 10 (2019) 1–24. https://doi.org/10.3389/fimmu.2019.02474.

[36] M.L. Oyen, Mechanical characterisation of hydrogel materials, Int. Mater. Rev. 59 (2014) 44–59. https://doi.org/10.1179/1743280413Y.0000000022.

[37] K.S. Anseth, C.N. Bowman, L. Brannon-Peppas, Mechanical properties of hydrogels and their experimental determination, Biomaterials 17 (1996) 1647–1657. https://doi.org/10.1016/0142-9612(96)87644-7.

[38] S.T. Koshy, R.M. Desai, P. Joly, J. Li, R.K. Bagrodia, S.A. Lewin, N.S. Joshi, D.J. Mooney, Click-Crosslinked Injectable Gelatin Hydrogels, Adv. Healthc. Mater. 5 (2016) 541–547. https://doi.org/10.1002/adhm.201500757.

[39] C.A. Schneider, W.S. Rasband, K.W. Eliceiri, NIH Image to ImageJ: 25 years of image analysis, Nat. Methods 9 (2012) 671–675. https://doi.org/10.1038/nmeth.2089.

[40] Z.Q. Liu, Scale space approach to directional analysis of images., Appl. Opt. 30 (1991) 1369–1373. https://doi.org/10.1364/AO.30.001369.

[41] J.B. Kelley, B.M. Paschal, Fluorescence-based quantification of nucleocytoplasmic transport, Methods 157 (2019) 106–114. https://doi.org/10.1016/j.ymeth.2018.11.002.

[42] C.H. Bucher, J.C. Berkmann, L.M. Burkhardt, C. Paschke, C. Schlundt, A. Lang, A. Wolter, A. Damerau, S. Geissler, H.D. Volk, G.N. Duda, K. Schmidt-Bleek, Local immune cell contributions to fracture healing in aged individuals – A novel role for interleukin 22, Exp. Mol. Med. 54 (2022) 1262–1276. https://doi.org/10.1038/s12276-022-00834-9.

[43] T.M. Ashhurst, F. Marsh-Wakefield, G.H. Putri, A.G. Spiteri, D. Shinko, M.N. Read, A.L. Smith, N.J.C. King, Integration, exploration, and analysis of high-dimensional single-cell cytometry data using Spectre, Cytom. Part A 101 (2022) 237–253. https://doi.org/10.1002/cyto.a.24350.

[44] M. Bao, J. Xie, N. Katoele, X. Hu, B. Wang, A. Piruska, W.T.S. Huck, Cellular Volume and Matrix Stiffness Direct Stem Cell Behavior in a 3D Microniche, ACS Appl. Mater. Interfaces 11 (2019) 1754–1759. https://doi.org/10.1021/acsami.8b19396.

[45] G. Devi, A.K. Hedger, R.J. Whitby, J.K. Watts, Double Click: Unexpected 1:2 Stoichiometry in a Norbornene–Tetrazine Reaction, J. Org. Chem. 88 (2023) 5341–5347. https://doi.org/10.1021/acs.joc.2c02861.

[46] S.B. Anderson, C.C. Lin, D. V. Kuntzler, K.S. Anseth, The performance of human mesenchymal stem cells encapsulated in cell-degradable polymer-peptide hydrogels, Biomaterials 32 (2011) 3564–3574. https://doi.org/10.1016/j.biomaterials.2011.01.064.

[47] D.M. Le, K. Kulangara, A.F. Adler, K.W. Leong, V.S. Ashby, Dynamic topographical control of mesenchymal stem cells by culture on responsive poly(Ïµ-caprolactone) surfaces, Adv. Mater. 23 (2011) 3278–3283. https://doi.org/10.1002/adma.201100821.

[48] S. Li, Y. Sun, Y. Chen, J. Lu, G. Jiang, K. Yu, Y. Wu, Y. Mao, H. Jin, J. Luo, S. Dong, B. Hu, Y. Ding, A. Liu, Y. Shen, G. Feng, S. Yan, Y. He, R. Yan, Sandwich Biomimetic Scaffold Based Tendon Stem/Progenitor Cell Alignment in a 3D Microenvironment for Functional Tendon Regeneration, ACS Appl. Mater. Interfaces 15 (2023) 4652–4667. https://doi.org/10.1021/acsami.2c16584.

[49] M. Ventre, F. Causa, P.A. Netti, Determinants of cell-material crosstalk at the interface: Towards engineering of cell instructive materials, J. R. Soc. Interface 9 (2012) 2017–2032. https://doi.org/10.1098/rsif.2012.0308.

[50] K.O. Okeyo, Y. Kibe, T. Adachi, Controlling macroscale cell alignment in self-organized cell sheets by tuning the microstructure of adhesion-limiting micromesh scaffolds, Mater. Today Adv. 12 (2021) 100194. https://doi.org/10.1016/j.mtadv.2021.100194.

[51] M. Werner, N.A. Kurniawan, G. Korus, C.V.C. Bouten, A. Petersen, Mesoscale substrate curvature overrules nanoscale contact guidance to direct bone marrow stromal cell migration, J. R. Soc. Interface 15 (2018). https://doi.org/10.1098/rsif.2018.0162.

[52] J. Knychala, N. Bouropoulos, C.J. Catt, O.L. Katsamenis, C.P. Please, B.G. Sengers, Pore geometry regulates early stage human bone marrow cell tissue formation and organisation, Ann. Biomed. Eng. 41 (2013) 917–930. https://doi.org/10.1007/s10439-013-0748-z.

869 [53] Y. Li, G. Huang, X. Zhang, L. Wang, Y. Du, T.J. Lu, F. Xu, Engineering cell alignment in vitro,
870 Biotechnol. Adv. 32 (2014) 347–365. https://doi.org/10.1016/j.biotechadv.2013.11.007.

871 [54] M. Murshed, Mechanism of bone mineralization, Cold Spring Harb. Perspect. Med. 8 (2018) 1–11.
872 https://doi.org/10.1101/CSHPERSPECT.A031229.

873 [55] M.S. Choudhery, R. Mahmood, D.T. Harris, F.J. Ahmad, Minimum criteria for defining induced
874 mesenchymal stem cells, Cell Biol. Int. 46 (2022) 986–989. https://doi.org/10.1002/cbin.11790.

875 [56] H. Busser, M. Najar, G. Raicevic, K. Pieters, R. Velez Pombo, P. Philippart, N. Meuleman, D. Bron, L.
876 Lagneaux, Isolation and Characterization of Human Mesenchymal Stromal Cell Subpopulations:
877 Comparison of Bone Marrow and Adipose Tissue, Stem Cells Dev. 24 (2015) 2142–2157.
878 https://doi.org/10.1089/scd.2015.0172.

879 [57] A. Valdivia, A.M. Avalos, L. Leyton, Thy-1 (CD90)-regulated cell adhesion and migration of
880 mesenchymal cells: insights into adhesomes, mechanical forces, and signaling pathways, Front. Cell
881 Dev. Biol. 11 (2023) 1–23. https://doi.org/10.3389/fcell.2023.1221306.

882 [58] L. Leyton, J. Díaz, S. Martínez, E. Palacios, L.A. Pérez, R.D. Pérez, Thy-1/CD90 a Bidirectional and
883 Lateral Signaling Scaffold, Front. Cell Dev. Biol. 7 (2019) 1–11.
884 https://doi.org/10.3389/fcell.2019.00132.

885 [59] A. Ode, J. Kopf, K. Schmidt-Bleek, P. Schrade, P. Kolar, F. Buttgereit, K. Lehmann, D. Hutmacher, G.
886 Duda, G. Kasper, CD73 and CD29 concurrently mediate the mechanically induced decrease of
887 migratory capacity of mesenchymal stromal cells, Eur. Cells Mater. 45 (2011) 26–42.

888 [60] S.A. Lund, C.M. Giachelli, M. Scatena, The role of osteopontin in inflammatory processes, J. Cell
889 Commun. Signal. 3 (2009) 311–322. https://doi.org/10.1007/s12079-009-0068-0.

890 [61] S. Bakhshandeh, U. Heras, H.M. Taïeb, A.R. Varadarajan, S.M. Lissek, S.M. Hücker, X. Lu, D.S.
891 Garske, S.A.E. Young, A. Abaurrea, M.M. Caffarel, A. Riestra, P. Bragado, J. Contzen, M. Gossen, S.
892 Kirsch, J. Warfsmann, K. Honarnejad, C.A. Klein, A. Cipitria, Dormancy-inducing 3D engineered
893 matrix uncovers mechanosensitive and drug-protective FHL2-p21 signaling axis, Sci. Adv. 10 (2024).
894 https://doi.org/10.1126/sciadv.adr3997.

895 [62] S.R. Caliari, S.L. Vega, M. Kwon, E.M. Soulas, J.A. Burdick, Dimensionality and spreading influence
896 MSC YAP/TAZ signaling in hydrogel environments, Biomaterials 103 (2016) 314–323.
897 https://doi.org/10.1016/j.biomaterials.2016.06.061.

898